

1 **Salivary gland macrophages and tissue-resident CD8⁺ T cells cooperate for homeostatic organ surveillance**

2

3 B. Stolp^{1,2,†}, F. Thelen^{1,†}, X. Ficht^{1,†}, L. M. Altenburger³, N. Ruef³, V. V. G. K. Inavalli^{4,5}, P. Germann^{6,7}, N. Page⁸,
4 F. Moalli⁹, A. Raimondi⁹, K. A. Keyser¹⁰, S. M. Seyed Jafari¹¹, F. Barone¹², M. S. Dettmer¹³, D. Merkler⁸, M.
5 Iannacone⁹, J. Sharpe^{6,7,14}, C. Schlapbach¹¹, O. T. Fackler², U. V. Nägerl^{4,5}, J. V. Stein^{3,*}

6

7 ¹Theodor Kocher Institute, University of Bern, 3012 Bern, Switzerland.

8 ²Department for Infectious Diseases, Integrative Virology, Center for Integrative Infectious Disease Research,
9 University Hospital Heidelberg, Im Neuenheimer Feld 344, 69120 Heidelberg, Germany.

10 ³Department of Oncology, Microbiology and Immunology, University of Fribourg, 1700 Fribourg, Switzerland.

11 ⁴University of Bordeaux, 33700 Bordeaux, France.

12 ⁵Interdisciplinary Institute for Neuroscience, CNRS UMR 5297, 33077 Bordeaux, France.

13 ⁶EMBL Barcelona, Dr. Aiguader 88, 08003 Barcelona, Spain.

14 ⁷Universitat Pompeu Fabra (UPF), 08002 Barcelona, Spain.

15 ⁸Department of Pathology and Immunology, University of Geneva, 1211 Geneva, Switzerland.

16 ⁹IRCCS San Raffaele Scientific Institute, 20132 Milan, Italy.

17 ¹⁰Institute for Virology, OE5230, Hannover Medical School, Carl-Neuberg-Str. 1, 30625 Hannover, Germany.

18 ¹¹Department of Dermatology, Inselspital, Bern University Hospital, University of Bern, Switzerland.

19 ¹²Institute of Inflammation and Ageing, University of Birmingham, Birmingham, United Kingdom.

20 ¹³Institute of Pathology, University of Bern, 3008 Bern, Switzerland.

21 ¹⁴Institució Catalana de Recerca i Estudis Avançats (ICREA), Pg. Lluís Companys 23, 08010 Barcelona, Spain.

22

23 † These authors contributed equally to this work

24 * To whom correspondence should be addressed

25 Contact: Jens V. Stein

26 Department of Oncology, Microbiology and Immunology

27 University of Fribourg

28

Ch. du Musée 5

29

CH-1700 Fribourg

30

email: jens.stein@unifr.ch

31

32 **One sentence summary**

33 Salivary gland tissue resident memory CD8⁺ T cells (T_{RM}) integrate complementary motility modes and

34 cooperate with tissue macrophages for homeostatic organ surveillance.

35

36 **Abstract**

37 It is well-established that tissue macrophages and tissue resident memory CD8⁺ T cells (T_{RM}) play important
38 roles for pathogen sensing and rapid protection of barrier tissues. In contrast, it is incompletely understood
39 how these two cell types cooperate for homeostatic organ surveillance after clearance of infections. Here,
40 we used intravital imaging to show that T_{RM} dynamically followed tissue macrophage topology in non-
41 inflamed murine submandibular salivary glands (SMG). Depletion of tissue macrophages interfered with SMG
42 T_{RM} motility and caused a reduction of interepithelial T cell crossing. Accordingly, in the absence of
43 macrophages, SMG T_{RM} failed to cluster in response to local inflammatory chemokines. A detailed analysis of
44 the SMG microarchitecture uncovered discontinuous attachment of tissue macrophages to neighboring
45 epithelial cells, with occasional macrophage protrusions bridging adjacent acini and ducts. When dissecting
46 the molecular mechanisms that drive homeostatic SMG T_{RM} motility, we found that these cells exhibit a wide
47 range of migration modes: in addition to chemokine- and adhesion receptor-driven motility, resting SMG T_{RM}
48 displayed a remarkable capacity for autonomous motility in the absence of chemoattractants and adhesive
49 ligands. Autonomous SMG T_{RM} motility was mediated by friction and insertion of protrusions into gaps
50 offered by the surrounding microenvironment. In sum, SMG T_{RM} display a unique continuum of migration
51 modes, which are supported *in vivo* by tissue macrophages to allow homeostatic patrolling of the complex
52 SMG architecture.

53

54 **Keywords**

55 Tissue-resident CD8⁺ T cells; non-lymphoid tissue; tissue macrophages; intravital imaging; super-resolution
56 shadow imaging; exocrine glands; chemokines; adhesion

57 **Introduction**

58 Naïve CD8⁺ T cells (T_N) continuously traffic through lymphoid tissue including peripheral lymph nodes (PLN)
59 and spleen, where they screen antigen presenting dendritic cells (DC) for the presence of cognate peptide-
60 MHC (pMHC) complexes. Intravital two-photon microscopy (2PM) of PLN uncovered a high amoeboid-like T_N
61 motility of 12-15 μm/min (1-4), facilitating their search for rare cognate pMHC-presenting DC interspersed
62 on a 3D stromal scaffold of fibroblastic reticular cells (FRC) (5-10). Intranodal motility is mediated by the CCR7
63 ligands CCL19 and CCL21 that drive F-actin polymerization at the leading edge in a Gαi-dependent manner
64 to generate a retrograde cortical actin flow. The integrin LFA-1 conveys cortical actin flow into forward
65 movement without generating substantial substrate adhesion (11). In the absence of homeostatic chemokine
66 signaling, T_N remain essentially immotile in *ex vivo* assays and show reduced scanning of lymphoid tissue *in*
67 *vivo* (11-16).

68 During viral infections, effector CD8⁺ T cells (T_{EFF}) generated in reactive lymphoid tissue disseminate into non-
69 lymphoid tissues (NLT) including gut, lung, genitourinary tract, and skin. T_{EFF} recruitment into NLT is mediated
70 by inflammatory chemokines and integrin ligands that guide these cells for killing of infected cells (17-19).

71 After clearance of viral antigens, T_{EFF} differentiate into CCR7⁺ central memory T cells (T_{CM}) and continue to
72 patrol lymphoid organs, or into effector memory T cells (T_{EM}) that lack CCR7 and CD62L expression and
73 recirculate through NLT (20). In addition, a subset of T_{EFF} differentiates into tissue-resident memory T cells
74 (T_{RM}), which stably reside in NLT and to a minor extent in lymphoid tissue as non-circulating, self-renewing
75 population. T_{RM} continuously patrol NLT in search of cognate pMHC on local cells and act as “first line”
76 sentinels to eliminate infected cells and to trigger an organ-wide alert status through cytokine secretion upon
77 pathogen re-encounter (19, 21-25).

78 The steady-state patrolling behavior of epidermal T_{RM} after clearance of infections has been extensively
79 studied in mouse models. Epidermal T_{RM} display characteristically elongated, dendritic shapes and move
80 with speeds of 1-2 μm/min in proximity to the extracellular matrix (ECM)-rich basement membrane (BM)
81 separating epidermis from dermis, i.e. in plane with the bottom keratinocyte layer (26, 27). A similar pattern
82 was recently confirmed in explanted human skin (28). Inhibition of Gαi receptor signaling induces epidermal
83 T_{RM} to round up and stop migrating, suggesting that similar to T_N, chemoattractants are essential for their

84 homeostatic search strategy (29). In addition, epidermal CD8⁺ T cells follow local chemokine signals to
85 accumulate around infected cells upon pathogen reencounter (30). Recent work has shown that such CD8⁺ T
86 cell accumulation is a critical step for cooperative elimination of infected stromal cells through repeated
87 cytotoxic attacks (31).

88 T_{RM} are also present in exocrine glands of the head and neck region, including submandibular salivary glands
89 (SMG). Salivary glands are targeted by several bacteria and viruses including human beta- and gamma-
90 herpesviruses, which can cause disease, mostly in immunocompromised individuals (32, 33). Like skin and
91 gut, SMG contains epithelial tissue basally anchored onto connective tissue. However, while skin and gut
92 consist of “layered” connective and epithelial tissue, the SMG epithelium displays a more complex 3D
93 “arborized” geometry. SMG acini secrete saliva into intermediate and collecting ducts, from where it is
94 channeled into the oral cavity via the Wharton’s duct (WD). The glandular epithelium is separated by a BM
95 from the supporting interstitium containing blood and lymphatic vasculature, fibroblasts and tissue
96 macrophages, which are dispersed throughout tissue (34). In tissue sections, most CD8⁺ T_{RM} in SMG are
97 localized within the abundant acini and ducts, implying a mechanism that allows T_{EFF} arriving in interstitial
98 venules to cross the BM underneath the epithelial compartment and develop into memory T cells (35, 36).
99 Yet, the cellular dynamics of homeostatic tissue surveillance by SMG T_{RM} and their interactions with other
100 local cell types have not been examined to date.

101 Here, we used intravital microscopy of mouse SMG in the memory phase following a systemic viral infection
102 to uncover a high baseline motility of resting T_{RM} of 6-7 μm/min. Remarkably, SMG T_{RM} followed tissue
103 macrophage topology during surveillance of SMG, and tissue macrophage depletion resulted in a significant
104 disruption of T_{RM} patrolling behavior. Using super-resolution microscopy to explore extracellular space
105 distribution in SMG, we observed discontinuous attachment of tissue macrophages to the surrounding tightly
106 packed epithelium, offering paths of least resistance to migrating T_{RM}. When examining the molecular
107 mechanism driving steady-state T_{RM} motility, we did not find compelling evidence for a decisive chemokine-
108 or integrin-driven contribution, in contrast to T_{CM} or epidermal T_{RM}. Instead, confinement alone was sufficient
109 to trigger SMG T_{RM} migration in the absence of chemoattractants and specific adhesion receptor
110 engagement. Mechanistically, the autonomous motility of resting SMG T_{RM} was mediated by friction- and

111 protrusion insertion-driven migration modes, while leaving cells responsive to extrinsic chemokine signals.
112 Taken together, our data uncover a new accessory role for tissue macrophages to support T_{RM} surveillance
113 of salivary glands. Our observations suggest a continuum of extrinsic factor-driven and cell-intrinsic motility
114 modes, which exploit topographic features of tissue macrophages to scan the complex 3D architecture of
115 exocrine glands during homeostatic surveillance.

116 **Results**

117 *Systemic viral infection leads to the establishment of T_{RM} in salivary glands*

118 We used a viral infection model for a comparative analysis of $CD8^+$ T cell populations in lymphoid tissue and
119 SMG (**Fig. S1A**). Systemic infection with lymphocytic choriomeningitis virus (LCMV)-OVA, a replication-
120 competent, attenuated LCMV mutant expressing ovalbumin (OVA) as model antigen (37), led to transient
121 and low viral titers in spleen on day 3 p.i. that remained below the detection limit in PLN and SMG (**Fig. S1B**).
122 Adoptively transferred GFP⁺ OT-I $CD8^+$ TCR tg T cells (which recognize the OVA₂₅₇₋₂₆₄ peptide in the context of
123 H2-K^b) (38) underwent a prototypic expansion – contraction kinetic in spleen and PLN over the course of 30
124 days (**Fig. S1, C and D**). Despite the lack of detectable viral titers, OT-I T cells accumulated in SMG from day
125 6 p.i. onwards, with a stable population maintained until at least day 30 p.i. (**Fig. S1, C and D**). By day 30 p.i.,
126 OT-I T cells isolated from SMG but not PLN or spleen showed increased expression of CD103 and CD69, while
127 losing the KLRG-1⁺ population present on day 6 p.i. (**Fig. S1, E and F**). These data suggest that most SMG $CD8^+$
128 T cells had developed into *bona fide* T_{RM} at day 30 p.i. (39). Memory OT-I $CD8^+$ T cells isolated from PLN were
129 approximately 65% $CD62L^+ CD44^{high} T_{CM}$, with the remaining population being $CD62L^- CD44^{high}$ memory T cells.
130 To take this heterogeneity into account, we refer to memory T cells isolated from PLN as T_{PLN-M} . T_{RM}
131 establishment in SMG was also observed at ≥ 30 day after systemic VSV-OVA infection. In sum, systemic viral
132 infection led to the recruitment and retention of $CD8^+$ T cell populations in SMG.

133
134 *Homeostatic SMG T_{RM} migration is characterized by dynamic cell shape changes*

135 We next determined the localization of T_{PLN-M} and T_{RM} in their target organs during the memory phase after
136 LCMV-OVA infection (**Fig. 1A**). Immunofluorescent sections showed that most GFP⁺ OT-I T cells in PLN and
137 SMG were dispersed evenly throughout tissue at day 30 p.i. (**Fig. 1B**). In PLN, OT-I T_{PLN-M} cells localized mainly
138 with smooth muscle actin (SMA)⁺ FRCs, whereas most OT-I T_{RM} cells in SMG were within or adjacent to
139 EpCAM⁺ acini and ducts (**Fig. 1B**). We developed a sequential surgery method to visualize homeostatic tissue
140 surveillance of T_{PLN-M} and T_{RM} in PLN and SMG, respectively, in the same host by 2PM (40). T_{PLN-M} displayed
141 characteristic amoeboid shapes and moved with high speeds similar to values reported for T_N (11.8 ± 4.0
142 $\mu\text{m}/\text{min}$, median \pm SD) (**Fig. 1, C and F to H; movie S1**). Compared to T_{PLN-M} , SMG T_{RM} displayed more

143 pronounced shape changes, with several protrusions probing the microenvironment during migration, at
144 times with thin and elongated cell bodies (**Fig. 1, D to G; movie S2**). While $T_{\text{PLN-M}}$ and T_{RM} covered large
145 distances throughout the observation period of intravital imaging sequences (20-60 min), both populations
146 differed in their speed and arrest coefficients, i.e. percentage of track segments with speeds $< 2.5 \mu\text{m}/\text{min}$.
147 Thus, SMG T_{RM} were significantly slower than $T_{\text{PLN-M}}$ (**Fig. 1H**) and had higher arrest coefficients (**Fig. 1I**).
148 Nonetheless, SMG T_{RM} retained a relatively high motility coefficient, which is a proxy of a cell's ability to scan
149 the environment during random migration, of $> 15 \mu\text{m}^2/\text{min}$ (**Fig. 1J**). Accordingly, their median speed of 6.8
150 $\pm 3.4 \mu\text{m}/\text{min}$ was notably higher than values reported for epidermal T_{RM} ($1-2 \mu\text{m}/\text{min}$) (26), with some cells
151 achieving speeds of $> 12 \mu\text{m}/\text{min}$. Both $T_{\text{PLN-M}}$ and SMG T_{RM} retained a fast response to antigenic stimulation,
152 as systemic administration of cognate peptide resulted in immediate arrest and secretion of $\text{IFN-}\gamma$ (**Fig. 1, J**
153 **and K**).

154 To examine a distinct CD8^+ T cell population, we transferred GFP^+ P14 CD8^+ TCR tg T cells (which recognize
155 the LCMV epitope gp_{33-41} in the context of H2-D^b) (41) and performed 2PM of PLN and SMG at > 30 days p.i.
156 with the LCMV Armstrong strain. We measured similar speeds and meandering indices for GFP^+ P14 $T_{\text{PLN-M}}$
157 and T_{RM} as with OT-I CD8^+ T cells, both before and after cognate peptide administration (**Fig. 1, L to N**).
158 Furthermore, GFP^+ OT-I T cells patrolled the structurally comparable lacrimal gland (LG) in the same speed
159 range as in SMG ($7.6 \pm 4.3 \mu\text{m}/\text{min}$, median \pm SD; **Fig 1O**). Collectively, these data suggest that migration
160 parameters of T_{RM} patrolling exocrine glands during homeostasis are independent of TCR specificity and may
161 reflect tissue properties.

162

163 *T_{RM} colocalize with tissue macrophages in salivary and lacrimal glands*

164 To explore the microenvironmental context of exocrine gland T_{RM} migration, we used a CD11c-YFP reporter
165 strain that preferentially labels CD64^+ SMG macrophages (**Fig. S2A**), as previously described (34). In tissue
166 sections, CD11c-YFP^+ cells were also positive for the macrophage marker Iba-1 , whereas some Iba-1^+ cells
167 were $\text{CD11c-YFP}^{\text{low/negative}}$, indicating that most but not all tissue macrophages were labeled in CD11c-YFP
168 mice (**Fig. S2 B**). Confocal analysis of thick tissue sections showed that CD11c-YFP^+ tissue macrophages
169 extended numerous protrusions from their cell bodies throughout the SMG tissue and were located within

170 EpCAM⁺ ducts and acini, as well as SMA⁺ perivascular structures of the interstitium (**Fig. S2C**). We further
171 investigated the spatial arrangement of macrophage protrusions with regard to epithelial BM markers. The
172 laminin ligand CD49f ($\alpha 6$) was prominent on the basal side of acini and to a lesser extent on ducts, which
173 were identified by the presence of the tight junction protein ZO-1 on the luminal side. In some cases, tissue
174 macrophage protrusions appeared to project between adjacent acini and ducts (**Fig. S2D**).

175 To assess the spatial relationship between tissue macrophages and T_{RM}, we transferred GFP⁺ OT-I T cells into
176 CD11c-YFP recipients one day prior to infection with LCMV-OVA and analyzed tissue sections by confocal
177 microscopy in memory phase (\geq day 30 p.i.). We observed a striking spatial proximity of T_{RM} and tissue
178 macrophages in SMG, with approximately 70% of OT-I T cells directly in contact with CD11c-YFP⁺ cells (**Fig. 2,**
179 **A and B; movie S3**). A comparable association of T_{RM} and tissue macrophages was observed in LG after LCMV-
180 OVA infection (**Fig. 2C**). The close spatial association between SMG tissue macrophages and T_{RM} was
181 confirmed by correlative light and electron microscopy imaging, with both cell membranes adjacent to each
182 other (**Fig. 2D**). Electron microscopy images also highlighted the compact tissue structure of acinar and ductal
183 epithelium linked by tight junctions and surrounded by a dense ECM (**Fig. 2E**). Occasionally, we observed
184 small T_{RM} clusters around tissue macrophages (**Fig. 2F**). CXCR3^{-/-} OT-I T_{RM} failed to accumulate at tissue
185 macrophage clusters, suggesting the existence of local CXCL9/CXCL10 “hotspots” at these sites (**Fig. 2F**).

186 Similarly, CD3⁺ T cells colocalized with CD68⁺ macrophages in human parotid gland sections, both as
187 dispersed individual cells and in clusters (**Fig. 2, G and H**). Taken together, T_{RM} displayed a prominent
188 colocalization with tissue macrophages in non-inflamed salivary glands across species.

189

190 *Migrating T_{RM} follow tissue macrophage topology during SMG surveillance*

191 The spatial proximity of T_{RM} to SMG macrophages in tissue sections raised the question whether patrolling
192 T_{RM} migrate alongside macrophages. 2PM imaging of GFP⁺ T_{RM} in LCMV-OVA memory phase CD11c-YFP
193 recipients indeed confirmed that T_{RM} crawled along CD11c-YFP⁺ macrophages during most of the observation
194 period, with T_{RM} shapes often closely matching the underlying macrophage topology. This was particularly
195 evident along thin macrophage protrusions, which T_{RM} often followed (**Fig. 3A; movie S4**). At the same time,
196 T_{RM} protrusions occasionally detached from macrophages, apparently scanning the surrounding

197 environment. Accordingly, we identified occasional T_{RM} track segments that were not associated with tissue
198 macrophages, with a minor reduction in T_{RM} speeds (7.0 ± 5.3 with versus 6.1 ± 4.8 $\mu\text{m}/\text{min}$ without
199 macrophages; $p < 0.001$).

200

201 *Depletion of tissue macrophages disrupts T_{RM} patrolling within and between acini and ducts*

202 Our observations prompted us to examine T_{RM} motility in the absence of tissue macrophages. To this end,
203 we generated bone marrow chimera by reconstituting C57BL/6 or Ubi-GFP mice with control CD11c-YFP or
204 CD11c-DTR bone marrow. At 6 weeks of reconstitution, we adoptively transferred GFP⁺ or DsRed⁺ OT-I T cells,
205 followed by LCMV-OVA infection. In some experiments, we directly transferred OT-I T cells into CD11c-DTR
206 mice and infected mice with LCMV-OVA. Both approaches allowed us to deplete CD11c⁺ macrophages by
207 diphtheria toxin (DTx) treatment in the memory phase without affecting the unfolding of the adaptive
208 immune response.

209 2PM imaging in DTx-treated mice revealed that SMG T_{RM} patrolling behavior was disrupted when
210 macrophages were depleted (**Fig. 3B**). T_{RM} motility was decreased, reflected by less displacement (**Fig. 3C**)
211 and slower speeds (**Fig. 3D**). Also, we observed cells that returned and migrated back the same path within
212 acini and ducts after macrophage depletion (**Fig. 3B; movie S5**). To quantify this behavior, we developed a
213 method to specifically retrieve U-turns from track parameters (**Fig. 3E**). This analysis confirmed that the
214 percent of T cell tracks showing U-turns was doubled in DTx-treated CD11c-DTR SMG from 8.1 to 16.7 % of
215 tracks (**Fig. 3F**). We observed a similar impact of macrophage depletion on T_{RM} speeds in LG (7.6 ± 4.3 and
216 5.5 ± 3.2 $\mu\text{m}/\text{min}$ in control and macrophage-depleted LG; $p < 0.001$), with a 2.5 fold increase in U-turns (**Fig.**
217 **S3, A and B**).

218 We next asked how impaired motility impacts organ surveillance. We generated tracks *in silico* from the data
219 sets obtained by 2PM imaging of DTx- and control-treated SMG and assessed the average T_{RM} dwell time in
220 a sphere of 80 μm diameter as surrogate epithelial structure (**Fig. 3E**). This analysis uncovered a nearly
221 threefold increased sphere dwell time from 24 ± 1.8 min for control SMG to 69 ± 6.5 min (median \pm SEM) for
222 DTx-treated CD11c-DTR SMG (**Fig. 3G**). A similar finding was made for control and macrophage-depleted LG

223 (Fig. S3C). Taken together, macrophage depletion disrupted motility parameters and increased the
224 propensity of T_{RM} to make U-turns.

225 226 *Absence of macrophages reduces T_{RM} movements into and out of epithelium*

227 We investigated whether lack of macrophages may also affect T_{RM} transitions into and out of epithelium as
228 part of the impaired motility pattern, as suggested by **movie S5**. To address this point, we reconstituted
229 irradiated Ubi-GFP mice expressing GFP in all cells with CD11c-YFP bone marrow before transfer of DsRed⁺
230 OT-I T cells and systemic LCMV-OVA infection. We found that in these chimera, acini and ducts of surgically
231 prepared SMG were GFP^{bright} and readily identifiable by their glandular shapes, whereas connective tissue
232 was GFP^{low}. Using case-by-case 3D rendering of 2PM image sequences in memory phase (≥ 30 days p.i. with
233 LCMV-OVA), we observed that DsRed⁺ T_{RM} were not restricted to individual epithelial structures but
234 occasionally crossed between adjacent acini or between epithelial and connective tissue compartments in a
235 bidirectional manner along macrophage protrusions (**Fig. 4A; movie S6**). We confirmed this observation in a
236 mouse model expressing membrane tomato and CD11c-YFP (**Fig. 4B**). In total, 75% of T_{RM} transits ($n = 42$)
237 into and out of epithelial structures occurred along macrophage protrusions (**Fig. 4C**). Given that not all tissue
238 macrophages are YFP⁺ (**Fig. S2B**), the actual percentage of macrophage-assisted transitions may still be
239 higher. DTx treatment of CD11c-DTR SMG reduced, but did not abolish, T_{RM} transit into or out of acini and
240 ducts. In total, we observed 55 T_{RM} crossing events into or out of acini in CD11c-YFP versus 12 events in
241 CD11c-DTR chimera SMG. These data corresponded to a 77% fewer crossing events per h track duration (**Fig.**
242 **4D**). Since this defect is more pronounced than the relatively mild decrease in T_{RM} speeds after macrophage
243 depletion (Fig. 3D), it is unlikely to be fully explained by decreased motility. Accordingly, when we normalized
244 T_{RM} transitions to migrated distance, we continued to observe impaired epithelial crossing in absence of
245 macrophages (Fig. 4E). Reduced T_{RM} crossing into and out of epithelial structures was also observed when we
246 prolonged DTx treatment for 5 days (**movie S7**).

247 248 *Impaired clustering of SMG T_{RM} after macrophage depletion*

249 We set out to interrogate the impact of macrophage – T_{RM} cooperativity in a local recall response. We
250 infected CD11c-YFP or CD11c-DTR mice with LCMV-OVA one day after transfer of GFP⁺ OT-I T cells and
251 depleted macrophages after 4 weeks using DTx (**Fig. S4A**). One day later, we re-challenged mice with an
252 mCherry- and OVA-expressing mouse cytomegalovirus (MCMV-OVAmCherry) (42, 43) administered locally
253 via retrograde WD injection. After 48 h, we analyzed SMG tissue sections for the presence and intensity of
254 viral foci identified by mCherry⁺ signal. This analysis confirmed the strictly local reinfection since no mCherry
255 signal was observed in the adjacent sublingual gland (**Fig. S4B**). We observed close proximity of OT-I T cells
256 and CD11c-YFP⁺ cells with MCMV-infected cells after SMG infection (**Fig. S4C**), with macrophages occasionally
257 engulfing infected cells (**Fig. S4D**). This observation is in line with the well-described macrophage core
258 function of engulfing apoptotic cells (efferocytosis) (44-47). Accordingly, we observed massively increased
259 numbers of infected cell foci in macrophage-depleted SMG after WD infection with MCMV-OVAmCherry as
260 compared to SMG containing tissue macrophages, irrespective of the presence of T_{RM} (**Fig. S4E**). Of note, in
261 the absence of tissue macrophages, T_{RM} partially suppressed viral replication as assessed by decreased
262 mCherry intensity in viral foci (**Fig. S4F**). Given the increased viral load after DTx treatment, tissue
263 macrophage depletion did not permit to directly assess the functional impact of reduced T_{RM} migration
264 patterns in presence and absence of these cells.

265 We therefore designed an experiment to examine T_{RM} cluster formation in response to exogenously added
266 inflammatory chemokine as a prerequisite for efficient elimination of infected cells (31). We treated LCMV-
267 OVA-immunized CD11c-YFP and CD11c-DTR BM chimera mice with DTx, followed one day later by local
268 injection of the CXCR3 ligand CXCL10 and quantum dots into SMG (**Fig. 4F**). We also administered anti- α 4
269 and LFA-1 blocking mAbs, which inhibit recruitment of circulating T cells to SMG (48). At 4 h after CXCL10
270 administration, we isolated SMG and quantified T_{RM} enrichment in thick confocal SMG sections according to
271 the area marked by the co-injected fluorescent quantum dots. CXCR3^{-/-} OT-I T cells did not show accumulation
272 in CXCL10 injection sites, supporting the specificity of chemokine-triggered clustering (49 - 63 > 500 μ m
273 versus 60 - 68 cells/cm² cells < 500 μ m from injection site; range from two SMG). WT OT-I T_{RM} were twofold
274 enriched at CXCL10 injection sites, suggesting that these cells had followed a CXCL10 gradient or became
275 retained during their surveillance path (**Fig. 4G**). In contrast, local accumulation of T_{RM} was lost when

276 macrophages had been depleted, although T_{RM} numbers outside the site of chemokine injection remained
277 comparable to macrophage-containing SMG (**Fig. 4G**). These data suggested that presence of SMG
278 macrophages permitted T_{RM} clustering in response to local inflammatory chemokines.

279
280 *Macrophages show discontinuous attachment to neighboring cells within SMG*

281 These observations prompted us to examine macrophage embedding within salivary gland tissue in more
282 detail. In immunofluorescent sections, most macrophage protrusions contained phosphotyrosine-positive
283 patches (**Fig. 5, A and B**), suggesting the presence of focal adhesion-like structures at these sites. We
284 investigated how these local signals correlated with macrophage attachment *in situ*. We applied the super-
285 resolution shadow imaging microscopy (SUSHI) technique, which was originally developed to visualize the
286 complex topology of the extracellular space (ECS) in living brain slices (49). SUSHI can also be used to follow
287 dynamic changes in ECS in response to a hyperosmotic challenge, which leads to cell shrinkage and ECS
288 widening in brain tissue. We adapted SUSHI imaging to acutely sliced SMG sections, which were superfused
289 with the cell-impermeable fluorescent dye Calcein in order to examine macrophage anchorage to adjacent
290 epithelium (**Fig. 5C**). Steady-state imaging revealed that the interstitium contained more ECS as compared to
291 the tightly packed epithelium (**Fig. 5, D and E**). We reasoned that SUSHI in combination with hyperosmotic
292 challenge could be applied to explore attachment between neighboring cells. Performing time-lapse ECS
293 imaging, we gradually increased the osmolarity to induce cell shrinkage, which led to a strong increase of ECS
294 in the interstitium (**movie S8**). In turn, interepithelial junctions remained relatively stable and only mildly
295 increased their spacing under osmotic challenge, reflecting the presence of adherens and tight junctions
296 known to link epithelial cells (**Fig. 5F**). In contrast, hyperosmolarity induced intraepithelial CD11c-YFP⁺
297 macrophages detachment from the adjacent epithelium (**Fig. 5, G and H**). This finding confirms previous
298 observations that tissue macrophages do not form continuous adhesive contacts with the epithelium, unlike
299 the extensive cell-to-cell contacts between acinar epithelial cells (50).

300 For an examination of macrophage protrusions and epithelial BM, we analyzed laminin-stained tissue
301 sections from immunized CD11c-YFP mice. We observed in some cases macrophage protrusions penetrating
302 between adjacent acini, or between epithelium and connective tissue, thus bridging adjacent compartments

303 separated by BM (**Fig. 5I; movie S9**). Using correlative confocal and transmission electron microscopy, we
304 validated that some macrophage protrusions transversed BM (**Fig. 5J**). Taken together, our data uncover
305 discontinuous attachment of tissue macrophages to neighboring cells and occasional incursions of
306 macrophage protrusions across the epithelial BM, creating paths of least resistance for migrating T_{RM} . These
307 observations offer an explanation for T_{RM} migration in accordance with tissue macrophage topography.

308

309 *In vivo motility of SMG T_{RM} remains largely intact upon integrin and chemokine receptor blockade*

310 Our data established a correlation between macrophage topography and T_{RM} migration patterns in non-
311 inflamed salivary and lacrimal glands. Next, we set out to dissect the molecular mechanisms that drive
312 homeostatic T_{RM} motility in SMG, focusing on well-described canonical chemoattractant- and integrin-
313 signaling pathways. We performed quantitative PCR analysis of cytokine and chemokine expression by
314 CD11c-YFP⁺ cells sorted from SMG in steady-state, acute (day 6 p.i.) and memory phase (day 30 p.i.) of LCMV-
315 OVA infection. We observed detectable mRNA levels of the cytokines IL-1 and TNF, as well as the chemokines
316 CCL3, CCL4, CXCL2, CXCL9, CXCL10 and CXCL16. Expression levels were similar at all time points analyzed,
317 reflecting the lack of detectable viral spread to this organ (**Fig. S1B**). Given the expression of promigratory
318 chemokines and adhesion receptors including ICAM-1 on tissue macrophages (51), we examined their
319 influence on T_{RM} migration parameters. Integrins mediate attachment and force transmission through
320 engagement of their ligands expressed by many cell types including macrophages. SMG T_{RM} express $\alpha 1$, $\alpha 4$,
321 αE , αL , $\beta 1$, $\beta 2$ and $\beta 7$ integrins, and low levels of αV (**Fig. S1 and S5A**). To assess their involvement in SMG
322 T_{RM} immune surveillance, we administered a mix of integrin-blocking mAbs against the major lymphocyte
323 integrin αL (CD11a/CD18, LFA-1), the E-cadherin receptor αE (CD103), and $\alpha 4$ (VLA-4 and $\alpha 4\beta 7$) to LCMV-
324 OVA memory phase mice containing T_{PLN-M} and T_{RM} (**Fig. 6A**). We confirmed that mAbs were saturating
325 surface integrins at the time point analyzed (**Fig. S5B**). We then followed OT-I T cell motility in PLN and SMG
326 on \geq day 30 p.i., using dual surgery 2PM of the same recipient mouse as above. Integrin blockade significantly
327 lowered T_{PLN-M} speeds from 11.7 to 8.8 $\mu\text{m}/\text{min}$ (**Fig. S5C**), similar to the decreased cell speeds of CD18-
328 deficient T_N in lymphoid stroma (16). In contrast, T_{RM} speeds and crawling along tissue macrophages
329 remained unaltered by this treatment (**Fig. 6, B and C; movie S10**). We did not detect Mac-1 (CD11b/CD18)

330 expression on SMG T_{RM} by flow cytometry, and addition of anti-Mac1 mAb to the integrin blocking mix did
331 not decrease T_{RM} speeds or guidance by tissue macrophages ($7.1 \pm 2.9 \mu\text{m}/\text{min}$). Similarly, inclusion of
332 blocking mAbs against $\alpha 1$ and αV together with αL , $\alpha 4$ and αE had no impact on T_{RM} cells speeds or
333 association with macrophages ($6.5 \pm 2.7 \mu\text{m}/\text{min}$).

334 Poor surface saturation of blocking anti- $\beta 1$ mAbs on OT-I T cells preempted us to assess the role of $\beta 1$
335 integrins for T_{RM} motility by this approach. As alternative, we directly administered the $\beta 1$ -blocking peptide
336 RGD or the control peptide RAD through the Wharton's duct (WD) into SMG and followed its impact on T_{RM}
337 motility parameters by 2PM. The WD channels saliva from SMG into the oral cavity and can be used to
338 administer reagents or pathogens through retrograde duct cannulation (52). Control experiments using WD
339 administration of OVA₂₅₇₋₂₆₄ peptide led to instantaneous arrest of T_{RM} similar to systemic injection,
340 suggesting efficient peptide permeation of SMG by this route. WD injection of either peptide slightly lowered
341 T_{RM} speeds; yet, we did not observe an impact on RGD administration on T_{RM} motility parameters as
342 compared to control peptide (**Fig. 6D**). This reflected low $\beta 1$ integrin levels in the interface between
343 macrophages and T_{RM} (**Fig. S5D**). Furthermore, E-cadherin levels on macrophages and T_{RM} were barely
344 detectable in SMG tissue sections, arguing against a role for this cadherin in mediating close spatial
345 association with tissue macrophages (**Fig. S5E**).

346 Cytokine-driven chemoattractant production plays a key role for T cell trafficking. Since the CXCR3 ligands
347 CXCL9 and CXCL10 play a role in T_{RM} clustering in SMG (**Fig. 2F**), we co-transferred WT and CXCR3^{-/-} OT-I T
348 cells one day prior to LCMV-OVA infection. Consistent with a recent report (48), we found that absence of
349 CXCR3 did not impair T_{RM} formation in SMG after viral infection. Non-clustered CXCR3^{-/-} OT-I T_{RM} showed no
350 significant differences in speeds as compared to WT T_{RM} (**Fig. 6E**), and lack of CXCR3 did not prevent T_{RM}
351 patrolling along tissue macrophages (**Fig. 2F**). These data argue against a role for CXCR3 in mediating baseline
352 homeostatic motility of SMG T_{RM}, despite its function in facilitating local clustering in response to
353 proinflammatory CXCR3 ligands (**Fig. 4F**).

354 To comprehensively assess a function for potential chemoattractants, we inhibited G α i signaling by systemic
355 PTx treatment (53) and performed 2PM analysis of OT-I T cell motility parameters on \geq day 30 after LCMV-
356 OVA infection. To control for inhibitor efficacy, we took advantage of the dual surgery of PLN and SMG in the

357 same recipient. Systemic PTx administration significantly slowed $T_{\text{PLN-M}}$ down from 11.3 $\mu\text{m}/\text{min}$ in control to
358 8.6 $\mu\text{m}/\text{min}$ in PTx-treated recipients (**Fig. S5F**), resembling observations made with PTx-treated T_{N} in PLN
359 (12, 15). Speeds were also decreased in SMG T_{RM} (from 6.6 to 5.5 $\mu\text{m}/\text{min}$) by PTx treatment (**Fig. 6F**),
360 suggesting a role for chemoattractants in mediating high T_{RM} speeds. Nonetheless, we observed a robust
361 residual motility and continued T_{RM} crawling along tissue macrophages in presence of PTx (**Fig. 6G, movie**
362 **S11**). Furthermore, PTx treatment had essentially no impact on U-turn frequency (1.15 fold increase as
363 compared to PTx_{mut}), in contrast to the absence of macrophages (**Fig. 3F**). These data suggest that while $G\alpha_i$ -
364 coupled receptors contribute to SMG T_{RM} motility, they are not required for T_{RM} association with tissue
365 macrophages. Finally, we interfered with MMP activity using the broad MMP-9, MMP-1, MMP-2, MMP-14
366 and MMP-7 inhibitor marimastat as described (87). Yet, MMP inhibition did not reduce T_{RM} migration speeds
367 (6.9 \pm 3.0 $\mu\text{m}/\text{min}$). Taken together, with exception of a minor effect by PTx, the *in vivo* inhibitor treatments
368 examined here did not alter T_{RM} motility and close spatial proximity to tissue macrophages.

369 To directly assess intercellular adhesion, we co-incubated freshly isolated tissue macrophages and T_{RM} *ex vivo*
370 and analyzed cluster formation by flow cytometry (**Fig. 6H**). As positive control, we pre-incubated
371 macrophages with cognate OVA₂₅₇₋₂₆₄ peptide. While addition of OVA₂₅₇₋₂₆₄ to tissue macrophages induced
372 detectable binding to T_{RM} , the baseline association between both populations remained low (**Fig. 6, H and I**).
373 Taken together, within the technical limitations of our experimental approach, our *in vivo* and *in vitro*
374 observations did not identify specific molecules that provide strong adhesion of resting SMG T_{RM} to tissue
375 macrophages. Our data rather suggested that T_{RM} association to macrophages occurred preferentially in the
376 context of the SMG microanatomy. Importantly, our data do not exclude the presence of unidentified
377 adhesion receptors mediating T_{RM} association to tissue macrophages *in vivo*.

378
379 *SMG T_{RM} motility is induced by confinement and can be tuned by extrinsic factors*

380 To address the molecular mechanisms underlying homeostatic T_{RM} motility, we employed under agarose
381 assays that allow to precisely control environmental factors and provide confinement required for T cell
382 motility (**Fig. 7A**) (11). To benchmark our system, we transferred T_{N} on CCL21 - and ICAM-1-coated plates as
383 surrogate lymphoid tissue microenvironment. We observed high chemokinetic T_{N} motility with similar speeds

384 as measured *in vivo* ($13.3 \pm 5.9 \mu\text{m}/\text{min}$) (**Fig. 7, B and C; movie S12**) (11, 16). Similarly, T_{RM} showed a high
385 motility ($11.4 \pm 3.0 \mu\text{m}/\text{min}$) when migrating on CXCL10 + CXCL12- and ICAM-1-coated plates, which was only
386 slightly lower than that of T_{N} (**Fig. 7C; movie S13**). These observations show that SMG T_{RM} respond to
387 inflammatory chemokines and adhesion molecules with high speeds.

388 Since we found that *in vivo* motility of resting T_{RM} was largely refractory to inhibition by PTx and integrins,
389 we examined T cell displacement on plates coated with fatty acid-free human serum albumin (HSA) and thus
390 free of chemoattractants and specific adhesion ligands. In line with previous findings (11), T_{N} and $T_{\text{PLN-M}}$
391 remained essentially immobile throughout the observation period (**Fig. 7, D to F; movies S14 and S15**). Under
392 these conditions, only 12% of T_{N} and 31% of $T_{\text{PLN-M}}$ migrated faster than $3 \mu\text{m}/\text{min}$, and showed low
393 directionality (**Fig. 7, G and H**). Remarkably, most SMG T_{RM} showed robust intrinsic motility on HSA-coated
394 plates despite the absence of chemoattractants and adhesion molecules (**Fig. 7, D to F; movies S14 and S15**).
395 Almost 70% of SMG T_{RM} migrated faster than $3 \mu\text{m}/\text{min}$ with high directionality, with their median speed of
396 $5.5 \mu\text{m}/\text{min}$ approaching values observed *in vivo* (**Fig. 7, G and H**). High temporal resolution imaging revealed
397 that migratory T_{RM} often formed several protrusions along the leading edge that appeared to probe the
398 environment, followed by rapid displacement of the cell body along one of the protrusions (**movie S16**).

399 Next, we performed under agarose assays in presence of SMG tissue macrophages to assess their influence
400 on T_{RM} motility. On the few occasions when motile T_{RM} contacted co-plated tissue macrophages, these
401 contacts were mostly transient (**Fig. 7, I and J**). Furthermore, T_{RM} did not crawl along macrophage protrusions
402 as observed *in vivo* (**movie S17**). These observations support the notion that T_{RM} - macrophage association
403 occurred preferentially in the SMG microenvironment.

404 We examined whether spontaneous motility was a common feature of all T_{RM} populations. To this end, we
405 isolated epidermal OT-I T cells from > 30 day LCMV-OVA-infected mice, which had been recruited to DNFB +
406 OVA₂₅₇₋₂₆₄-treated skin during the expansion phase. In line with the reported sensitivity to *in vivo* PTx
407 treatment (29), epidermal T_{RM} did not show spontaneous motility in the absence of chemokine (**Fig. 7, K and**
408 **L; movie S18**), although these cells remained responsive to exogenous chemokines ($5.6 \pm 4.2 \mu\text{m}/\text{min}$ in
409 presence of CXCL10 and CXCL12). Thus, confinement alone was sufficient to induce spontaneous SMG but
410 not epidermal T_{RM} migration, representing to the best of our knowledge the first observation of such a

411 motility mode in resting T cells. Their speeds were increased in presence of chemokines and adhesion
412 molecules, suggesting that extrinsic promigratory factors tune intrinsic cell motility.

413

414 *Friction mediates SMG T_{RM} migration in the absence of chemokines and ICAM-1*

415 We set out to characterize the requirements for autonomous SMG T_{RM} motility using under agarose assays.
416 Reflecting the absence of chemoattractants and integrin ligands, pertussis toxin (PTx) treatment or addition
417 of the β 1-blocking peptide RGD did not affect T_{RM} speeds in this setting (**Fig. 7M**). Although Mac-1 binds
418 weakly to serum albumin (54), addition of anti-Mac-1 mAb did not cause a significant reduction in T_{RM} speeds
419 (**Fig. 7M**). These observations suggested a friction-based migration mechanism (55). Friction is the resisting
420 force when two elements slide against each other and may be composed of a number of fundamental forces.
421 While the nature of the weak interactions between T_{RM} and migratory surface causing friction are not
422 defined, we hypothesized that these might in part involve bivalent cations. Indeed, chelation of bivalent
423 cations by EDTA caused a strong decline of T_{RM} speeds under agarose (**Fig. 7M**). High temporal resolution
424 imaging showed that despite the lack of translocation in presence of EDTA, SMG T_{RM} continued to probe the
425 environment via transient protrusion formation, essentially “running on the spot” (**Fig. 7, N and O; movie**
426 **S19 left**). This behavior precipitated a loss in the motility coefficient (**Fig. 7P**). In sum, our data suggest that
427 bivalent cation-dependent friction between SMG T_{RM} and the confining 2D surfaces generated sufficient
428 traction for translocation in the absence of considerable surface binding.

429

430 *SMG T_{RM} insert protrusions between adjacent structures for translocation*

431 In addition to friction-based migration, protrusion insertion has emerged in recent years as a complementary
432 mechanism to allow cell migration without specific adhesions (55). The continuous probing of T_{RM} in presence
433 of EDTA (**Fig. 7N**) provided an opportunity to test whether topographic features of the environment such as
434 narrow intercellular spaces may rescue cell motility by permitting insertion of pseudopods as mechanical
435 “footholds” (56, 57). As a surrogate approach to re-introduce a “2.5D” environmental geometry in under
436 agarose assays, we co-transferred a surplus of T_N together with T_{RM} and performed time-lapse imaging in the
437 presence of EDTA and in the absence of chemoattractants and adhesion molecules (**Fig. 8A**). Remarkably,

438 T_{RM} localized within T_N clusters frequently showed lateral displacement despite the presence of EDTA (**movies**
439 **S19, right, and S20**). Under these conditions, T_{RM} displacement occurred through insertion of protrusions
440 between adjacent T_N and subsequent translocation of the cell body accompanied by dynamic cell shape
441 changes (**Fig. 8B**). T_{RM} within T_N clusters were significantly faster than isolated T_{RM} (5.8 ± 3.0 and 2.3 ± 1.7
442 $\mu\text{m}/\text{min}$, respectively), displayed higher directionality, and resembled in cell shape and speeds T_{RM} migrating
443 *in vivo* (**Fig. 8, C to E**). Once T_{RM} had traversed T_N clusters, they returned to their probing behavior without
444 efficient translocation, indicating a close interdependence on physical contact and motility (**movie S19 right**).
445 We then examined whether potential residual molecular interactions between naive T cells and T_{RM} might
446 act as drivers of migration. We therefore transferred uncoated polystyrene beads with T_{RM} in under agarose
447 assays. These beads replaced T_N as surrogate 2.5D structures and allowed to examine protrusion insertion in
448 the absence of potential adhesive interactions. In this setting, T_{RM} recapitulated the behavior observed within
449 T_N clusters, showing effective cell displacement only when in contact with clusters of beads for protrusion
450 insertion (**Fig. 8F; movie S21**). T_{RM} speeds increased to $6.4 \pm 1.9 \mu\text{m}/\text{min}$ and became more directional when
451 in contact with beads, whereas isolated T_{RM} showed no displacement (**Fig. 8, G and H**). This was also seen
452 when beads were passivated with pluronic acid, which prevents any unspecific residual adhesion. We further
453 observed that T_{RM} moved around dense bead areas, in line with a search for permissive gaps for locomotion
454 (**movie S21**). In sum, our data uncover the remarkable ability of resting SMG T_{RM} to migrate by adapting to
455 topographic features of the environment through protrusion insertion and shape deformation, even in the
456 absence of considerable friction, chemoattractants and adhesion receptors (**Fig. 8I**). At the same time, these
457 data are consistent with the notion that these cells retain responsiveness to chemokine signals, follow
458 macrophage topology to short-cut SMG epithelium and accumulate at local inflammatory hot-spots upon
459 pathogen re-encounter (**Fig. 8J**).

460 **Discussion**

461 After clearing of pathogens, T_{RM} display a remarkable capacity to patrol heterogeneous tissues without
462 impairing vital organ functions (21-25). Their scanning behavior evolved because T cells are MHC-restricted
463 and hence need to physically probe membrane surfaces of immotile stromal cells. In this study, we examined
464 how these cells achieve this feat in the complex arborized epithelial structure of SMG during homeostatic
465 immune surveillance. Our main finding is that T_{RM} preferentially moved along tissue macrophages, and that
466 depletion of macrophages impaired T_{RM} patrolling. These observations assign a new accessory role to tissue
467 macrophages in addition to their core functions for tissue homeostasis and sentinels of infection. Our data
468 suggest two non-exclusive options to explain macrophage guidance of T_{RM}: first, through unidentified specific
469 adhesive interaction(s) independent of ICAM-1 and other canonical adhesion molecules such as CD103; and
470 second, by offering paths of least resistance within the exocrine gland microenvironment for protrusion
471 insertion by autonomously moving T cells. Our data provide support for the second option without discarding
472 the first one. Thus, reductionist *in vitro* experiments revealed that SMG T_{RM} respond to exogeneous cues
473 from chemoattractant and adhesion molecules. At the same time, confinement alone suffices to trigger
474 friction- and protrusion insertion-based motility without exogeneous chemoattractants or adhesion
475 molecule. The continuum of intrinsic motility and integration of external factors may permit T_{RM} to patrol
476 these exocrine glands in homeostasis and rapidly respond to inflammatory stimuli.

477 Macrophages and T cells closely cooperate during the onset of inflammation, the effector phase and
478 contraction through antigen presentation, cytokine secretion and effector functions such as phagocytosis.
479 Yet, little is known whether and how these two cell types collaborate for surveillance of NLT during
480 homeostasis. Tissue macrophages are best characterized for their core function of maintenance or
481 restoration of tissue homeostasis by engulfing apoptotic cells, clearing debris, initiation of repair and cloaking
482 of microlesions (44-47, 58, 59). Furthermore, tissue macrophages serve as sentinels of infection, leading to
483 cytokine secretion and leukocyte recruitment (21, 60, 61). In recent years, several non-phagocytic and non-
484 sentinel functions were assigned to macrophages, as it was recognized that core functions of parenchymal
485 parts of organs became outsourced to accessory cells. Accessory macrophage functions include blood vessel
486 and mammary duct morphogenesis, hematopoietic stem cell maintenance, pancreatic cell specification, lipid

487 metabolism, relay of long-distance signals during zebrafish patterning and electric conduction in the heart
488 (62, 63). Our data suggest a novel accessory function, which is to facilitate T_{RM} patrolling within and between
489 acini and ducts of arborized secretory epithelium.

490 Our initial assumption was that specific adhesion receptors drive T cell association with tissue macrophages,
491 while chemoattractants fuel their high baseline motility. Tissue macrophage express ICAM-1 and other
492 adhesion molecules that can serve as ligands for T cell adhesion receptors, as well as chemoattractants (51).
493 It was therefore startling that - against our expectations - we were unable to find evidence for strong adhesive
494 contacts between salivary gland macrophages and T_{RM}. The experimental systems we have used to address
495 this point encompass *in vivo* inhibition of adhesion receptors in combination with reductionist *in vitro*
496 adhesion assays. Such assays have previously been employed to identify intercellular adhesion through
497 specific molecular interactions, such as ICAM-1-driven binding between T cells and DCs (64). It is important
498 to note our data do not rule out the presence of specific adhesive and/or promigratory interactions between
499 T_{RM} and tissue macrophages *in situ*. For instance, low T_{RM} binding to tissue macrophages *in vitro* may be owing
500 to altered gene expression patterns after macrophage isolation (65). Along the same line, we have not
501 examined talin-deficient T cells lacking functional integrins, since these cells are unable to attach to
502 endothelium for extravasation. Poor surface mAb saturation preempted a complete analysis of CD44 for SMG
503 T_{RM} motility (66). Finally, PTx treatment induced a minor but significant reduction in T_{RM} speeds *in vivo*. Yet,
504 PTx treatment had essentially no impact on U-turn frequency and movement along tissue macrophages. In
505 line with this, recent observations suggest that guidance and adhesion do not necessarily correlate, as T_N
506 migrate along the FRC network even in the absence of LFA-1 and CCR7 (11). Finally, the fact that isolated T_{RM}
507 can move between polystyrene beads or other lymphocytes for efficient translocation, correlating with
508 spontaneous formation of intercalating protrusions, suggests that any structure with permissive gaps can
509 serve for topological guidance. Nonetheless, owing to a lack of a suitable experimental system, our data do
510 not provide unambiguous evidence for or against specific molecular interactions between T_{RM} and
511 macrophages *in vivo*. Therefore, we cannot definitely clarify to which extent specific interactions and
512 microenvironmental architecture contribute to macrophage – T_{RM} association *in situ*.

513 The canonical model of leukocyte migration postulates chemoattractant-stimulated F-actin polymerization
514 at the leading edge (4). The resulting retrograde F-actin flow in turn generates traction and cell body
515 translocation via an integrin “clutch” that binds to adhesion receptors of the ECM or on the surface of
516 neighboring cells. Although integrin-independent migration in 3D matrices has become a widely accepted
517 concept in cell biology based on studies with cell lines and DCs (55), several studies uncovered integrin
518 involvement during immune surveillance of skin T cells (29, 67). Thus, it remained unclear to which extent
519 integrin-free motility occurs in primary lymphocytes, which have less cytoplasm and surface area as
520 compared to DCs and cell lines. Another open question was whether memory T cells from distinct anatomical
521 locations would employ similar or tissue-specific mechanisms of host surveillance. Work by Zaid et al. has
522 identified a critical role of G-protein-coupled receptor signaling during scanning by epidermal T_{RM} (29). Our
523 own observations confirm that similar to T_N and T_{PLN-M}, *ex vivo* confined epidermal T_{RM} do not migrate in the
524 absence of integrin ligands or chemoattractants. Spontaneous motility under 2D confinement appears to
525 constitute therefore a distinctive hallmark of SMG T_{RM} not shared by other resting T cells. Isolated T_{RM} showed
526 high intrinsic protrusive activity *in vitro*, which may reflect high F-actin turnover and/or increased Rho-ROCK-
527 mediated actomyosin contractility. Constitutive protrusion formation could be driven by increased activity
528 of actin nucleation factors at the leading edge, supported by forward cytoplasm flow driven by uropod
529 contractions. In fact, low adhesiveness under confinement induces spontaneous amoeboid motility via
530 cortical contractility in adherent mesenchymal cell lines (68, 69), suggesting that T_{RM} may use a similar
531 mechanism for autonomous migration *in vitro* and *in vivo*. Yet, it remains currently unknown how this unique
532 motility program is imprinted in SMG T_{RM} and whether it is shared by tissue-resident cells from other exocrine
533 glands.

534 Adhesion-free motility in 2D conditions has been proposed for large, blebbing carcinoma cells, based on
535 friction mediated by a large interface between migrating cells and substrates (70). We show that 2D
536 confinement suffices to induce T_{RM} motility through cation-dependent friction, since these cells become
537 unable to translocate their cell bodies in presence of EDTA. Friction is composed of multiple nanoscale forces
538 between two interfaces. For instance, electrostatic and van der Waals forces have been implicated in cell
539 migration and non-specific adherence to substrate (71-73). As chelation of bivalent cations reduced friction

540 below a threshold for cell translocation in our setting, electrostatic forces are likely to be relevant. In this
541 context, transmembrane molecules may require bivalent cations for force transmission in the absence of
542 specific counter-ligands. In principle, cells may compensate for a lower friction by increasing the contacting
543 surface area (74). However, lymphocytes are likely too small to generate a sufficiently large interface under
544 these conditions. In turn, T_{RM} regained the capability to translocate in presence of EDTA when narrow spaces
545 are created by immotile neighboring cells or beads that lack strong adhesion to each other. This motility
546 mode correlated with continuous changes in cell shapes owing to the intrinsic protrusion formation capacity
547 of T_{RM} . Thus, T_{RM} continuously formed multiple simultaneous protrusions that probed the environment,
548 leading to their insertion into permissive gaps and subsequent cell body translocation. How T_{RM} protrusions
549 generated tractive force for cell translocation under these conditions remains incompletely understood. One
550 possibility is that protrusions insert into gaps of the 3D environment akin to cogs of a cogwheel and transmit
551 the necessary force for translocation through retrograde actin flow along irregularly shaped surfaces, even
552 in the absence of any adhesive interaction. In fact, this translocation mode is reminiscent of the “squeezing
553 and flowing” mechanism proposed for DCs (75), although SMG T_{RM} do not require a chemokine gradient for
554 displacement. We also observed that T_{RM} avoided areas of high bead density, thus choosing the path of least
555 resistance in this mode.

556 The efferocytic function of tissue macrophages conceivably requires physical contact with surrounding cells
557 to detect and phagocytose senescent or infected cells. Our data are in line with a model where the flexible
558 anchorage of macrophage protrusions between epithelial cells facilitates the insertion of F-actin-rich
559 pseudopods by T_{RM} before squeezing of the nucleus as biggest organelle (55, 57, 76). T_{RM} migration along
560 macrophages may be further assisted by unknown adhesion receptors or other molecular interactions
561 between these cells. In any event, non-proteolytic path finding is beneficial to preserve the integrity of the
562 target tissue, as it does not require constant repair of newly generated discontinuities in the ECM (77). The
563 scanning strategy adopted by T_{RM} resembles the migration pattern of T cell blasts in 3D collagen networks,
564 where these cells routinely bypass dense collagen areas, while probing the environment for permissive gaps
565 for cell body translocation (78). The influence of the physical properties of the microenvironment is
566 increasingly recognized to play a central role for decision-taking by migrating leukocytes (71). Thus,

567 leukocytes have recently been shown to use the nucleus to identify the path of least resistance in complex
568 3D environments with different pore sizes (79). This migration mode preserves tissue integrity and is
569 energetically favorable by avoiding ECM degradation. Yet, technical limitations in recreating the complex
570 tissue microenvironment of exocrine glands under controlled *in vitro* conditions limit the experimental scope
571 to address this issue in depth.

572 Our local CXCL10 deposition experiment suggests that macrophages facilitate local T_{RM} accumulation at sites
573 where inflammatory chemokines are produced. This resembles observations made in skin infection models
574 where CXCR3 promotes CD8⁺ T cell accumulation at sites of viral replication necessary for efficient elimination
575 of infected cells (18, 19). A recent study by Förster and colleagues has uncovered an unexpectedly low killing
576 rate of cytotoxic T cells against viral-infected stromal cells (80). Thus, effective stromal cell elimination
577 requires cooperativity through repeated cytotoxic attacks by multiple CD8⁺ T cells. Conceivably, the
578 promigratory accessory function of tissue macrophages described here helps to cluster a quorum of T_{RM} for
579 successful stromal cell killing. Furthermore, unlike the monoclonal T_{RM} population created in our
580 experimental setting, not all T_{RM} recognize the same pathogen under physiological conditions. This imposes
581 a requirement for T cells to scan local sites of pathogen re-emergence and to form clusters for timely
582 elimination of fast-replicating microbes. In line with these observations, presence of macrophages and T_{RM}
583 cooperatively reduced viral load in the MCMV challenge model through efferocytosis of infected cells and
584 reduction of viral replication, partially owing to presence of T_{RM}. Given that SMG macrophages are poor cross-
585 presenters (34), these data are consistent with the concept of macrophage-aided tissue scanning by T_{RM}.
586 Furthermore, both cell types are likely to enhance antiviral response through secretion of interferons and
587 other cytokines.

588 In sum, our data assign a previously unnoticed cooperativity between tissue-resident innate and adaptive
589 immune cell populations. These findings uncover a noticeable capacity of SMG T_{RM} to integrate a continuum
590 of intrinsic and external signals, friction and 3D structures for efficient motility, providing these cells with
591 maximal flexibility for NLT surveillance. We propose that such a mode of tissue patrolling is ideally adapted
592 to the arborized epithelial architecture of exocrine glands by permitting homeostatic surveillance while
593 maintaining responsiveness to local inflammatory cues.

594 **Materials and Methods**

595 *Mice*

596 OT-I TCR (38) and P14 TCR transgenic mice (41) were backcrossed to Tg(UBC-GFP)30Scha “Ubi-GFP” (81) or
597 hCD2-dsRed (82) mice. Ubi-GFP (GFP⁺) OT-I mice backcrossed to CXCR3^{-/-} mice have been described (83).
598 Tg(Itgax-Venus)1Mnz CD11c-YFP (84) and Tg(Itgax-DTR/EGFP)57Lan CD11c-DTR mice were used as recipients
599 or bone marrow donors for lethally irradiated C57BL/6 or Ubi-GFP mice. C57BL/6 mice were purchased from
600 Janvier (AD Horst). All mice were maintained at the Department of Clinical Research animal facility of the
601 University of Bern, at the Theodor Kocher Institute and the University of Fribourg. All animal work has been
602 approved by the Cantonal Committees for Animal Experimentation and conducted according to federal
603 guidelines.

604

605 *T cell transfer and viral infections*

606 CD8⁺ T cells were negatively isolated from spleen, peripheral and mesenteric lymph nodes of GFP⁺ or dsRed⁺
607 OT-I or GFP⁺ P14 mice, using the EasySep™ Mouse CD8⁺ T cell Isolation Kit (Stem Cell Technologies). CD8⁺ T
608 cell purity was confirmed to be > 95% by flow cytometry prior to cell transfer. 10⁴ OT-I T cells were i.v.
609 transferred into recipient mice 24 h before i.p. infection with 10⁵ pfu LCMV-OVA (37). For epidermal T_{RM}, we
610 injected 5 x 10⁴ OT-I as above, and 15 µl 0.3% DNFB (in acetone/oil 4:1) was applied to the right flank on day
611 3 p.i., followed by 500 ng SIINFEKL peptide days 4 and 5 p.i.. Experimental read-outs for the acute, cleared
612 and memory phase of viral infection were performed 6, 15 and ≥ 30 days p.i., respectively.

613

614 *LCMV virus titer*

615 C57BL/6 mice were infected i.p. with 10⁵ pfu LCMV-OVA and sacrificed 3 or 5 days later. PLN, spleens and
616 SMG were harvested and organs were snap frozen in liquid nitrogen. Recombinant LCMV-OVA infectivity was
617 measured by immunofocus assay on MC57 cells as previously described⁹⁶.

618

619 *Antibodies and reagents*

620 Alexa633-conjugated anti-PNAd MECA79, α L-integrin FD441.8 and anti- α 4-integrin PS/2 mAbs were from
 621 nanotools (Freiburg, Germany). Anti- α 1-integrin Ha31/8 was from BD Bioscience, anti- α 4 integrin PS/2 and
 622 anti- α E integrin M290 were from BioXCell, anti- α V integrin RMV-7 was from BioLegend, and anti-Mac1 mAb
 623 M1/70 was purified from hybridoma supernatant. TexasRed-Dextran 70 kDa was from Molecular Probes.
 624 Cascade Blue (MW 10 kDa) was purchased from Invitrogen. TRITC-Dextran (MW 70 kDa) and Diphtheria Toxin
 625 whereas purchased from Sigma. Pertussis toxin (PTx) and enzymatically inactive mutant PTx (PTx_{mut}) were
 626 obtained from List Biological Laboratories. Sodium Pyruvate (100 mM; #11360-039), HEPES buffer (1M;
 627 #15630-056), Minimum essential Medium Non-essential amino acids (MEM NEAA, #11140-035), L-Glutamine
 628 (200 mM; #25030-024), PenStrep (#15140-122) and RPMI-1640 (#21875-034) were purchased from Gibco
 629 and Fetal Bovine Serum (FCS, #SV30143.03) was purchased from HyClone.

630

631 *Flow cytometry analysis*

632 PLN and spleen were harvested at the indicated time points and single cell suspensions were obtained by
 633 passing organs through cell strainers (70 μ m; Bioswisstec). Red blood cell lysis was performed on splenocytes
 634 in some experiments. For analysis of SMG and LG, organs were minced and treated with 2 U/ μ l collagenase
 635 II (Worthington Biochem), 2 U/ μ l bovine DNase I (Calbiochem) and - only for intracellular stainings of
 636 cytokines – 5 μ g/ml Brefeldin A (B6542, Sigma-Aldrich) in CMR (RPMI/10% FCS/1% HEPES/1% PenStrep/2
 637 mM L-Glutamine/1 mM Sodium Pyruvate) for 30 min at 37°C, passed through a 70 μ m cell strainer and
 638 washed with PBS/5 mM EDTA. We used following reagents for flow cytometry:

Antibody	clone	company	Order number
anti-CD3-APC	145-2C11	Biolegend	100312
anti-CD8a-PE	53-6.7	BD Biosciences	553033
anti-CD8a-PerCP	53-6.7	Biolegend	100732
anti-CD8a-APC/Fire750	53-6.7	Biolegend	100766
anti-CD11a-PE	M17/4	Biolegend	101107
anti-CD11b-PE	M1/70	BD Biosciences	553311

anti-CD11c-APC	HL3	BD Biosciences	550261
anti-CD18-PE	M18/2	Biolegend	101407
anti-CD29-PE	HM β 1-1	Biolegend	102207
anti-CD44-PE	IM7	BD Biosciences	553134
anti-CD45-PerCP	30-F11	BD Bioscience	557235
anti-CD45-BV711	30-F11	Biolegend	103147
anti-CD45.1-AF488	A20	Biolegend	110718
anti-CD45R/B220-APC	RA3-6B2	Biolegend	103212
anti-CD49a-PE	HM α 1	Biolegend	142603
anti-CD49b-Biotin	DX5	Biolegend	108903
anti-CD49d-PE	PS/2	Southern Biotech	1520-09L
anti-CD51-PE	RMV-7	Biolegend	104105
anti-CD64-AF647	X54-517	BD Bioscience	558539
anti-CD69-PE	H1.2F3	Biolegend	104508
anti-CD103-APC	2E7	Biolegend	121414
anti-CD103-Biotin	M290	BD Bioscience	557493
anti- β 7-integrin-Biotin	FIB504	Biolegend	321209
anti-F4/80-FITC	BM8	Biolegend	123108
anti-F4/80-APC	BM8	Biolegend	123116
anti-KLRG1-PE	2F1	BD Bioscience	561621
anti-KLRG-1-PE-Cy7	2F1	Biolegend	138415
anti-KLRG1-APC	2F1	Biolegend	138411
anti-NK1.1-APC	PK136	Biolegend	108710
anti-Siglec-F-PE	E50-2440	BD Bioscience	562068
Streptavidin-APC	-	Biolegend	405207
anti-rat IgG1 K-APC	-	Biolegend	400412

armenian hamster IgG-PE	-	Biolegend	400907
-------------------------	---	-----------	--------

639 Single cell suspensions were stained for surface antigens on ice for 30 min with the indicated antibodies and
640 washed in FACS buffer (FB; PBS/2% FCS/1 mM EDTA) or FB with 5 µg/ml Brefeldin A for intracellular cytokine
641 stainings. All sample were washed in FB after staining, and for intracellular stainings, cells were permeabilized
642 and fixed in Cytofix/Cytoperm (#51-2090KZ, BD Biosciences) for 20 min on ice. Fixative was removed by
643 washing with Perm/Wash buffer (#51-2091KZ, BD Biosciences) and subsequent intracellular staining steps
644 were performed in Perm/Wash buffer. Cells were washed again prior to acquisition and at least 10⁵ cells in
645 the lymphocyte FSC/SSC gate were acquired using a FACSCalibur (BD Bioscience), LSR II (BD Bioscience), LSR
646 II SORP Upgrade (BD Bioscience) or Attune NxT Flow cytometer (ThermoFisher). Total cell counts were
647 obtained by measuring single cell suspensions in PKH26 reference microbeads (Sigma) for 1 min at high
648 speed. Gating for CD103⁺ and KLRG1⁺ was set according to isotype controls. For CD69 staining, positive and
649 negative gates were set according to distinguishable populations and FMO was subtracted from the final %
650 of CD69⁺ cells as background.

651

652 *Immunofluorescence*

653 Mice were anesthetized with i.p. injection of ketamine and xylazine and perfused with ice-cold 1% PFA.
654 Organs were harvested and fixed overnight in 2% PFA prior to embedding in TissueTek O.C.T. compound
655 (Sakura) for cryostat sectioning or 5% low-melting-point agarose (Sigma) for vibratome (Microslicer™ DTK-
656 1000) sectioning. 6 µm-thick frozen cryostat sections were permeabilized, blocked and stained with 0.05%
657 Triton-X 100 in 5% skimmed milk or 0.05% Tween 20 and 3% BSA for 1h, washed 3 times with PBS/1%
658 BSA/0.05% Tween (TBPBS) and stained with goat-anti-Iba1 1/200 (ab5076, Abcam) and anti-phosphotyrosine
659 (pTyr) (ab179530, Abcam) for 2 h at RT prior to mounting with Fluoromount-G (Electron Microscopy
660 Sciences).

661 For vibratome sections, 100 µm-thick section were collected in a 48-well plate and blocked with TBPBS for 2
662 h, then blocked with F_c-block o.n. at 4°C (hybridoma supernatant; 2.4 mg/ml diluted 1/800 in TBPBS). After
663 washing once with TBPBS for 1 h, sections were stained in TBPBS for 2-3 days at 4°C (in 100 µl, 3 sections per
664 well) with Alexa647-conjugated anti-EpCAM (1/160 dilution; clone G8.8, 118212, Biolegend), eFluor660-

665 conjugated anti-E-cadherin (1/200 dilution; clone DECMA-1, 50-3249-1633, eBioscience), polyclonal rabbit
666 anti-Laminin (1/1000 dilution; Z0097, Dako) or Cy3-conjugated anti- α -smooth muscle cell actin (clone 1A4,
667 C6198, Sigma). Sections were washed 3 times for 1 h with TBPBS and incubated with secondary Cy3-
668 conjugated anti-rabbit Ig (1/400 in TBPBS; 111-165-144, Jackson Immune Research), then washed 3 times 1
669 h with TBPBS and one time with PBS. Images were acquired with a Zeiss LSM510 or Leica SP5 confocal
670 microscope and processed using Adobe Photoshop CS6 and Imaris 8.4.1. We used Imaris software for surface
671 rendering and channel masking function to separate fluorophores with close emission spectra (i.e. GFP and
672 YFP).

673

674 *2PM image acquisition and analysis*

675 2PM intravital imaging of the popliteal lymph node was performed as described (85). In brief, mice were
676 anesthetized with ketamine/xylazine/acepromazine. The right popliteal lymph node was surgically exposed.
677 Prior to recording, Alexa 633-conjugated MECA-79 (10 μ g/mouse) was injected i.v. to label HEV. 2PM was
678 performed with an Olympus BX50WI microscope equipped with a 20X Olympus (NA 0.95) or 25X Nikon (NA
679 1.0) objective and a TrimScope 2PM system controlled by ImSpector software (LaVisionBiotec). Some of the
680 image series were acquired using an automated system for real-time correction of tissue drift (86). For 2-
681 photon excitation, a Ti:sapphire laser (Mai Tai HP) was tuned to 780 or 840 nm. For 4-dimensional analysis
682 of cell migration, 11 to 20 x-y sections with z-spacing of 2-4 μ m (22-64 μ m depth) were acquired every 20 s
683 for 20-60 min; the field of view was 150-350 x 150-350 μ m. Emitted light and second harmonic signals were
684 detected through 447/55-nm, 525/50-nm, 593/40-nm and 655/40-nm bandpass filters with non-descanned
685 detectors in case of C57BL/6 recipient mice. For CD11c-YFP⁺ recipient mice or bone marrow chimera, we used
686 447/55-nm, 513/20-nm, 543/30-nm and 624/30-nm bandpass filters.

687 For imaging of the SMG, neck and thorax of the mouse were shaved, and residual hair removed with hair
688 removal cream (Veet). Subsequently, the animal was fixed on its back onto a custom-built SMG imaging stage
689 and stereotactic holders were attached to the head for stabilization. A 10 x 5 mm piece of skin on the right
690 side of the neck was excised to expose the right SMG lobe, which was micro-surgically loosened from
691 surrounding tissue. The right SMG lobe was flipped to the right and gently immobilized in between 2 cover

692 glasses to minimize motion artifacts from heartbeat and breathing. During the whole operation and imaging
693 procedure tissue was kept moist. During imaging, the temperature at the SMG was monitored and kept at
694 37°C by a heating ring. In most experiments, mice were operated twice (for PLN and SMG) in alternating
695 order to directly compare behavior of cells in different organs of the same recipient. Prior to imaging, blood
696 vessels were labeled by i.v. injection of 400 – 600 µg of 10 kDa Cascade-blue dextran or 70 kDa TexasRed
697 Dextran. Surgical exposure of the LG was essentially performed as for the SMG, with the mouse fixed on its
698 left flank onto the custom-built SMG imaging stage and a 10 x 5 mm piece of skin excised between the right
699 ear and eye of the mouse.

700 Sequences of image stacks were transformed into volume-rendered four-dimensional videos with Volocity
701 6.0 or Imaris 6.00-9.00 (Bitplane), which was also used for semi-automated tracking of cell motility in three
702 dimensions. Drift in image sequences was corrected using a MATLAB script recognizing 3D movement in a
703 reference channel or by using the correct drift function of Imaris. Since our filter set up does not allow
704 complete separation of GFP and YFP signals, we performed spectral unmixing of GFP and YFP using the Image
705 J plugin “Spectral_Unmixing” from Joachim Walter. Cellular motility parameters were calculated from x, y,
706 and z coordinates of cell centroids using Volocity, Imaris and MATLAB protocols. The motility coefficient, a
707 measure of the ability of a cell to move away from its starting position, was calculated from the gradient of
708 a graph of mean displacement against the square root of time. We defined U-turns as the steepest turn over
709 five steps of a track, if it is over more than 166 degrees and has a skew line distance between the first and
710 last step smaller than one mean step of the respective track (**Fig. 7D**) to exclude continuous turns. The given
711 binomial proportion 95% confidence intervals are Wilson Score intervals. We generated 100 synthetic tracks
712 of 12 h duration for each condition using a sampling strategy, which was designed to preserve the correlation
713 between velocity and turning angle and the autocorrelation of velocity and turning angle (10). We then took
714 the first timestep further than 40 µm away from the origin of each track as simulated dwelling time in an
715 acinus of 80 µm diameter. These analyses were performed using scientific computing packages for Python.

716 For the image series depicted in the Figures, raw 2PM data was filtered with a fine median filter (3x3x1), and
717 brightness and contrast were adjusted. Shape factors were determined by rendering and tracking cells in

718 Imaris, and manually excluding all cells that did not move along a horizontal axis. The signal from the filter
719 cells was projected into a single z-slice and the shape-factor of the 2D image calculated with Volocity.

720

721 *In vivo inhibitor treatment*

722 Gai signaling by chemokines was blocked as described previously (53). Briefly, mice were treated with 3 µg
723 PTx or PTx_{mut} by i.p. injection 3 h prior to imaging. For depletion of CD11c-positive cells in CD11c-DTR mice
724 or BM chimera, 4 ng/g Diphtheria Toxin (DTx) was i.p. injected 24 h prior to imaging. Depletion efficiency of
725 CD11c⁺ cells was determined by flow cytometry and was above 98% in all organs analyzed. For the
726 synchronous blocking of integrins, 100 µg each of the purified mAbs M290, FD441.8, M1/70 and PS/2 were
727 injected i.v. 16 h prior to imaging. Surface saturation of blocking mAbs in PLN and SMG suspensions was
728 determined at the end of the experiment by sample staining with or without the same mAb clones used for
729 blocking, followed by a fluorescently labeled secondary mAb and flow cytometry. RGD peptide or as control
730 GRADSP (RAD) peptide (SIGMA) was injected via Wharton's duct cannulation (approximately 600 nmol of
731 either peptide in 30 µl per lobe in PBS), as described previously (52). For this procedure, mice were
732 anesthetized with ketamine/xylazine and their upper incisors rested on a metal rod and the lower incisors
733 pulled down with string, which kept the mouth open. With the aid of a stereomicroscope, we located the
734 orifice of the Wharton's duct in the sublingual caruncle and inserted a pointed glass-capillary (Untreated
735 Fused Silica Tubing - L × I.D. 3 m × 0.10 mm, #25715, Sigma). The glass capillary was connected to a Hamilton
736 Micro-syringe (Hamilton) via fine bore polythene tubing (0.28 mm, #800/100/100, Smiths), which allowed
737 the injection of small volumes. For inhibition of MMPs, Marimastat (#S7156) was obtained from Sellcheck
738 and diluted in PBS/10% DMSO (0.2 mg/g) or the corresponding volume of PBS/10% DMSO was injected i.p.
739 90 min before starting imaging (87). OVA₂₅₇₋₂₆₄ (#BAP-201) and gp₃₃₋₄₁ (#BAP-206) peptides were obtained
740 from ECM microcollections and 200 µg/100 µl saline injected i.v. immediately prior to imaging or 6 - 12 h
741 prior to organ harvest for FACS staining.

742

743 *Viral infection via Wharton's duct cannulation*

744 Wharton's duct cannulation was prepared as described above. Approximately 12500 pfu MCMV-
745 OVA_{mCherry} (42) were injected into the Wharton's duct (WD) of DTx-treated CD11c-DTR or CD11c-YFP mice
746 in memory phase of LCMV-OVA infection. Mice were euthanized 48 h post infection and SMG tissue fixed in
747 4% PFA at 4°C for 12 h.

748

749 *Under agarose assays*

750 T_N were isolated from spleen and PLN of a naive mouse using CD8⁺ T cell isolation kit from Stemcell. For
751 epidermal T_{RM}, skin on the right flank was harvested, minced and digested in 1 ml 0.25% Trypsin-EDTA
752 (25200056, gibco) 30 min at 37°C. Trypsin was inactivated with FCS and the skin was passed through a 70 µm
753 cell strainer and washed with PBS/5 mM EDTA. For under agarose experiments comparing SMG versus
754 epidermal T_{RM}, SMG T_{RM} were treated in exactly the same way (digestion with Trypsin-EDTA). SMG-derived
755 macrophages were isolated from uninfected CD11c-YFP mice and sorted for CD11c-YFP⁺ cells. T_{RM} and T_{CM}
756 were isolated from SMG and PLN, respectively, from LCMV-OVA-infected C57BL/6 mice in memory phase.
757 Single cells suspension of SMG and PLN were stained with APC-conjugated anti-KLRG1 mAb and sorted for
758 GFP⁺ or DsRED⁺ KLRG1⁻ T_{RM} and T_{PLN-M}, respectively. A 17-mm diameter circle was cut into the center of 60-
759 mm dishes. The hole was sealed from the bottom part of the dish using aquarium silicone (Marina) and a 24-
760 mm glass coverslip. After the silicone dried, we overlaid a 5 mm-high ring cut from a 15-ml falcon tube and
761 sealed the borders with low melting point paraffin. Coverslips were washed with PBS and coated with 3%
762 human serum albumin (HSA; A1653, Sigma) o.n. at 4°C or for 3 h at 37°C. In some experiments, coverslips
763 were coated with 10 µg/ml fibronectin (11080938001, Roche315-02, PeproTech). Fresh medium was added
764 every 2 days and macrophages were cultured for 6-7 days. For naïve T cell migration, coverslips were coated
765 with 20 µg/ml Protein A (6500-10, BioVision) for 1 h at 37°C, washed 3 times with PBS and blocked with 1.5
766 % BSA for 2 h at 37°C or o.n. at 4°C. After washing once with PBS, cover glasses were coated for 2 h at 37°C
767 with 100 nM recombinant ICAM1-F_C (796IC, R&D Systems) and washed 2 times with PBS. Five ml of 2 x HBSS
768 and 10 ml of 2 x RPMI containing 1% HSA for T_{RM} and T_{CM} and 20% FBS for macrophage and naïve T cell
769 experiments, were mixed and heated in a water bath to 56°C. Golden agarose (100 mg; 50152, Lonza) was
770 dissolved and heated in 5 ml distilled water before adding to the prewarmed medium to give a 1% agarose

771 mix. After cooling to 37°C, 500 µl of the agarose mix was added on top of the coverslip. In some cases,
772 inhibitors were added (200 µg/ml PTx, 5 µg/ml anti-Mac1 mAb, 10 µM RGD or GRADSP, 2.5 mM EDTA, or 5
773 µg/ml Hoechst (H21492, Invitrogen). After incubation for 30 min at 4°C, the dish was warmed up to 37°C
774 before adding 1 ml of PBS outside the ring to prevent agarose drying. We punched a sink hole (diameter
775 approximately 2 mm) at the side of the agarose. Sorted T cell populations were suspended in RPMI/0.5% HSA
776 and in some cases treated with 5 µg anti-Mac1, 10 µM RGD or GRADSP, and pelleted in an Eppendorf tube.
777 Cells were resuspended in the smallest possible achievable volume (ca. 5-10 µl) and 0.3 µl were injected in
778 the opposite side from the sink hole using a 2.5-µl Eppendorf pipette. In some experiments, polystyrene
779 beads (Sigma-Aldrich, LB30 or 78462) were co-injected with the cells. From the sink hole surplus of medium
780 was collected to confine cells between the agarose and the glass slide. Time-lapse images were taken from
781 the center of the dish using a Zeiss fluorescent microscope (AxioObserver, Zeiss).

782

783 *Correlative Confocal and Transmission Electron Microscopy*

784 Correlative confocal and transmission electron microscopy (TEM) was carried out as described (88). Briefly,
785 CD11c-YFP mice were perfused with PBS and SMG were fixed *in situ* by left ventricle injection of 1.5%
786 glutaraldehyde/2% PFA in 0.1 M sodium cacodylate buffer (pH 7.4). SMG were harvested and immersed in
787 the same solution for 16 h. Fixed samples were cryoprotected in 30% sucrose prior to embedding in OCT and
788 freezing. Thirty µm sections were cut with a CM1520 cryostat (Leica) and collected on Superfrost Plus slides
789 (Thermo Fisher Scientific). Sections were processed for confocal imaging using PBS as mounting medium to
790 prevent dehydration. After confocal image acquisition, the coverslips were gently removed and sections
791 adherent to the slide were processed for TEM as described (88). Briefly, sections were postfixed using the
792 ferrocyanide-reduced osmium-thiocarbohydrazide-osmium (R-OTO) procedure, *en bloc* stained in 1% uranyl
793 acetate and dehydrated through increasing concentration of ethanol. Finally, sections were embedded by
794 overlaying a BEEM capsule filled with Epoxy resin. The BEEM capsules containing the embedded sections
795 were detached by immersing the slides in liquid nitrogen, leaving the section facing up on the resin block.
796 The specimens were mounted on a Leica Ultracut UCT and 70-90 nm thick serial sections were collected on
797 formvar-coated copper slot grids and imaged with a ZEISS Leo912AB Omega fitted with a 2k × 2k bottom-

798 mounted slow-scan Proscan camera controlled by the EsivisionPro 3.2 software. Using the florescent confocal
799 and bright field images, the same areas were relocated in the electron microscope and several images were
800 acquired through the different serial section. Acquired TEM images were then aligned and overlaid with the
801 confocal images by means of the eC-CLEM Icy plugin (89).

802

803 *Super-resolution shadow imaging (SUSHI)*

804 After euthanizing mice with CO₂, submandibular salivary glands (SMG) were isolated from 8-11 weeks old
805 C57BL6 or CD11c-YFP mice and submerged in ice-cold PBS. SMG were embedded in 4% low gelling agarose
806 (Sigma), cut in 300 µm-thick transversal slices and submerged in cold complete RPMI medium containing:
807 10% FCS (Hyclone). Slices were left to recover at room temperature for 15-30 min before entering the imaging
808 chamber of a custom-built 3D-STED microscopy setup (49). First, the positively labelled (YFP) macrophages
809 were identified at a depth of 20-30 µm below the surface and imaged in STED mode (excitation 485 nm,
810 depletion 597 nm, objective HC PL APO 63X/1.30 NA, Leica) with the following acquisition parameters: field
811 of view: 200 µm X 200 µm; pixel size: 48 nm X 48 nm; pixel dwell time: 30 µs, frame acquisition time: 20 min.
812 The medium was exchanged in the chamber with the complete RPMI containing 400 µM Calcein dye, which
813 was allowed for 20 - 30 min to disperse throughout the extracellular space of the tissue. Subsequently, we
814 acquired a SUSHI image to identify a region of interest around the macrophages. We performed a
815 hyperosmolar challenge by exchanging the chamber solution (300 µl) with high osmolar solution (350
816 mOsm/L), and acquired time lapse images to track changes in ECS topology with a 20-min interval between
817 the image frames. All image analysis including morphological measurements were done on raw images using
818 the "Plot Line Profile" function in ImageJ on structures of interest. Brightness and contrast were adjusted
819 using the "Brightness and Contrast" function in ImageJ. It was applied for illustration purposes only and did
820 not affect the quantitative analysis. No filtering or any other image processing was applied, other than
821 inverting the look-up-tables (LUT). The YFP signal was used only to identify macrophages and was not
822 recorded during subsequent imaging. Only unambiguously recognizable macrophages and ECS were
823 analyzed. Image analysis was performed on SMG slices from two mice in two independent experiments.

824

825 *Confocal imaging of the p-Tyr signal and quantification*

826 Mice were perfused with PBS containing 4% paraformaldehyde, SMG were isolated and fixed in the same
827 solution at 4°C for 18 h, followed by at least 5 h dehydration in 30% sucrose. Glands were embedded in OCT
828 (Tissue-Tek) and cut at a thickness of 6 and 20 µm at the cryostat, flash dried and fixed with 4% PFA for 10
829 min at room temperature. Sections were permeabilized using 0.2% Triton X-100, blocked in 10% serum of
830 the secondary antibody and 2% BSA containing PBS and stained with antibodies for 18 h at 4°C in the same
831 solution, after being washed in PBS and mounted in Prolong Gold containing DAPI (Invitrogen, Carlsbad, CA).
832 Fluorescence microscopy was performed using the LSM880 confocal microscopes with 40x oil (Plan-
833 Apochromat 40x 1.3 Oil DIC M27) or 63x oil (Plan-Apochromat 63x 1.3 Oil DIC M27) objectives (Zeiss,
834 Oberkochen, Germany). All images were recorded using sequential excitation. The lack of spectral overlap
835 was confirmed using single fluorescing specimens and antibody specificity via secondary controls.
836 Macrophages were identified via iba-1 and the presence and location of p-Tyr signal was quantified in 7 fields
837 of view using Imaris software. Brightness and contrast were adjusted for each image individually. Gaussian
838 filters were applied using Imaris software.

839

840 *Chemokine-driven T_{RM} accumulation*

841 After 6 weeks of reconstitution with CD11c-YFP or CD11c-DTR BM, we transferred 10^4 GFP⁺ OT-I T cells and
842 infected the day after with 10^5 pfu LCMV-OVA. After ≥ 30 days p.i., mice were anesthetized one day after i.p.
843 injection of DTx (4 ng/g) as for 2PM imaging. To block immigration of cells from blood, we treated mice with
844 integrin blocking antibodies anti- α L (FD441.8) and anti- α 4 (PS/2) (each at 50 µg/mouse; nanotools). SMG
845 was surgically exposed. Using thin glass capillaries as for Wharton's duct injection, we injected 2 µl of a 1:1
846 mix of mCXCL10 (100 µg/ml; R&D 466-CR-010) and Qdots₆₅₅ (0.16 µM; Thermo Fisher Q2152MP), to obtain
847 a final mCXCL10 amount of 0.5 µg per site of injection. After 4 h, we sacrificed the mice and harvest the SMG
848 for vibratome sectioning. Mosaic images were taken of 100 µm-thick sections, and lobes with the highest
849 Qdot signal were analyzed by transforming the 3D image into extended 2D image, using the Z-projection
850 function of ImageJ. T_{RM} density in the surrounding area and injection area (defined as an octagon with 500
851 µm diameter) was calculated using Imaris 8.4.1.

852

853 *Statistical analysis*

854 Two-tailed, unpaired Student's t-test, Mann-Whitney U-test, one-way ANOVA with Dunnett's multiple
855 comparisons test, Kruskal-Wallis test, or a Wilcoxon rang test was used to determine statistical significance
856 (Prism, GraphPad). Significance was set at $p < 0.05$.

857 **Acknowledgements**

858 We thank Dr. Marcus Thelen (IRB, Bellinzona) for support with confocal imaging. This work benefitted from
859 optical setups of the Microscopy Imaging Center of the University of Bern and of the Biolmaging platform of
860 the University of Fribourg.

861

862 **Funding**

863 This work was funded by Swiss National Foundation (SNF) project grants 31003A_135649, 31003A_153457
864 and 31003A_172994 (to JVS), Leopoldina fellowship LPDS 2011-16 (to BS) and SFB1129 (to BS and OTF), and
865 the Novartis foundation fellowship 16C193 (to FT). PG and JS acknowledge support of the Spanish Ministry
866 of Economy and Competitiveness, “Centro de Excelencia Severo Ochoa 2013-2017” and support of the CERCA
867 Programme/Generalitat de Catalunya.

868

869 **Author contributions**

870 BS, FT and XF performed most experiments with support by LMA and NR. LMA and KI carried out SUSHI
871 imaging under supervision of UVN. PG carried out computational analysis under supervision of JS. AR and FM
872 performed correlative electron microscopy of SMG sections under supervision of MI. NP, KAK, FB, DM and
873 OTF provided vital material and support. SMSF, MSD and CS analyzed human SMG sections. BS, FT, XF and
874 JVS designed experiments and wrote the manuscript with input from all coauthors.

875

876 **Competing interests**

877 The authors declare no competing interests.

878

879

880 **References**

- 881 1. R. N. Germain, M. J. Miller, M. L. Dustin, M. C. Nussenzweig, Dynamic imaging of the immune system:
882 progress, pitfalls and promise. *Nature Publishing Group*. **6**, 497–507 (2006).
- 883 2. C. Sumen, T. R. Mempel, I. B. Mazo, U. H. von Andrian, Intravital microscopy: visualizing immunity in
884 context. *Immunity*. **21**, 315–329 (2004).
- 885 3. B. Breart, P. Bousso, Cellular orchestration of T cell priming in lymph nodes. *Current Opinion in*
886 *Immunology*. **18**, 483–490 (2006).
- 887 4. P. Friedl, B. Weigelin, Interstitial leukocyte migration and immune function. *Nat Immunol*. **9**, 960–969
888 (2008).
- 889 5. M. Bajénoff *et al.*, Highways, byways and breadcrumbs: directing lymphocyte traffic in the lymph
890 node. *Trends in Immunology*. **28**, 346–352 (2007).
- 891 6. T. Katakai, K. Habiro, T. Kinashi, Dendritic Cells Regulate High-Speed Interstitial T Cell Migration in the
892 Lymph Node via LFA-1/ICAM-1. *J. Immunol*. **191**, 1188–1199 (2013).
- 893 7. M. Lee, J. N. Mandl, R. N. Germain, A. J. Yates, The race for the prize: T-cell trafficking strategies for
894 optimal surveillance. *Blood*. **120**, 1432–1438 (2012).
- 895 8. G. Bogle, P. R. Dunbar, Agent-based simulation of T-cell activation and proliferation within a lymph
896 node. *Immunol Cell Biol*. **88**, 172–179 (2009).
- 897 9. J. Textor *et al.*, Random Migration and Signal Integration Promote Rapid and Robust T Cell
898 Recruitment. *PLoS Comput Biol*. **10**, e1003752–16 (2014).
- 899 10. M. Ackerknecht *et al.*, Antigen Availability and DOCK2-Driven Motility Govern CD4+ T Cell Interactions
900 with Dendritic Cells In Vivo. *The Journal of Immunology*. **199**, 520–530 (2017).
- 901 11. M. Hons *et al.*, Chemokines and integrins independently tune actin flow and substrate friction during
902 intranodal migration of T cells. *Nat Immunol*. **19**, 606–616 (2018).

- 903 12. T. Okada, J. G. Cyster, CC chemokine receptor 7 contributes to Gi-dependent T cell motility in the
904 lymph node. *J. Immunol.* **178**, 2973–2978 (2007).
- 905 13. T. Worbs, T. R. Mempel, J. Bölter, U. H. von Andrian, R. Förster, CCR7 ligands stimulate the intranodal
906 motility of T lymphocytes in vivo. *J. Exp. Med.* **204**, 489–495 (2007).
- 907 14. I.-Y. Hwang, C. Park, J. H. Kehrl, Impaired trafficking of Gnai2^{+/-} and Gnai2^{-/-} T lymphocytes:
908 implications for T cell movement within lymph nodes. *J. Immunol.* **179**, 439–448 (2007).
- 909 15. F. Asperti-Boursin, E. Real, G. Bismuth, A. Trautmann, E. Donnadieu, CCR7 ligands control basal T cell
910 motility within lymph node slices in a phosphoinositide 3-kinase-independent manner. *J. Exp. Med.*
911 **204**, 1167–1179 (2007).
- 912 16. E. Woolf *et al.*, Lymph node chemokines promote sustained T lymphocyte motility without triggering
913 stable integrin adhesiveness in the absence of shear forces. *Nat Immunol.* **8**, 1076–1085 (2007).
- 914 17. U. H. von Andrian, C. R. Mackay, T-cell function and migration. Two sides of the same coin. *New*
915 *England Journal of Medicine.* **343**, 1020–1034 (2000).
- 916 18. H. D. Hickman *et al.*, CXCR3 chemokine receptor enables local CD8(+) T cell migration for the
917 destruction of virus-infected cells. *Immunity.* **42**, 524–537 (2015).
- 918 19. S. Ariotti *et al.*, Subtle CXCR3-Dependent Chemotaxis of CTLs within Infected Tissue Allows Efficient
919 Target Localization. *The Journal of Immunology.* **195**, 5285–5295 (2015).
- 920 20. F. Sallusto, J. Geginat, A. Lanzavecchia, Central memory and effector memory T cell subsets: function,
921 generation, and maintenance. *Annu Rev Immunol.* **22**, 745–763 (2004).
- 922 21. N. Iijima, A. Iwasaki, A local macrophage chemokine network sustains protective tissue-resident
923 memory CD4 T cells. *Science.* **346**, 93–98 (2014).
- 924 22. J. M. Schenkel *et al.*, Resident memory CD8 T cells trigger protective innate and adaptive immune
925 responses. *Science.* **346**, 98–101 (2014).

- 926 23. G. Stary *et al.*, A mucosal vaccine against *Chlamydia trachomatis* generates two waves of protective
927 memory T cells. *Science*. **348**, aaa8205–aaa8205 (2015).
- 928 24. S. Ariotti *et al.*, Skin-resident memory CD8⁺ T cells trigger a state of tissue-wide pathogen alert.
929 *Science*. **346**, 101–105 (2014).
- 930 25. M. Kadoki *et al.*, Organism-Level Analysis of Vaccination Reveals Networks of Protection across
931 Tissues. *Cell*, 1–38 (2017).
- 932 26. A. Zaid *et al.*, Persistence of skin-resident memory T cells within an epidermal niche. *Proc. Natl. Acad.*
933 *Sci. U.S.A.* **111**, 5307–5312 (2014).
- 934 27. S. Ariotti *et al.*, Tissue-resident memory CD8⁺ T cells continuously patrol skin epithelia to quickly
935 recognize local antigen. *Proceedings of the National Academy of Sciences*. **109**, 19739–19744 (2012).
- 936 28. F. E. Dijkgraaf *et al.*, Tissue patrol by resident memory CD8⁺ T cells in human skin. *Nat Immunol.* **20**,
937 756–764 (2019).
- 938 29. A. Zaid *et al.*, Chemokine Receptor-Dependent Control of Skin Tissue-Resident Memory T Cell
939 Formation. *The Journal of Immunology*. **199**, 2451–2459 (2017).
- 940 30. J. W. Griffith, C. L. Sokol, A. D. Luster, Chemokines and Chemokine Receptors: Positioning Cells for
941 Host Defense and Immunity. *Annu Rev Immunol.* **32**, 659–702 (2014).
- 942 31. S. Halle, O. Halle, R. Förster, Mechanisms and Dynamics of T Cell-Mediated Cytotoxicity In Vivo. *Trends*
943 *Immunol.* **38**, 432–443 (2017).
- 944 32. C. S. Miller *et al.*, High Prevalence of Multiple Human Herpesviruses in Saliva from Human
945 Immunodeficiency Virus-Infected Persons in the Era of Highly Active Antiretroviral Therapy. *Journal*
946 *of Clinical Microbiology*. **44**, 2409–2415 (2006).
- 947 33. M. J. Cannon *et al.*, Repeated measures study of weekly and daily cytomegalovirus shedding patterns
948 in saliva and urine of healthy cytomegalovirus-seropositive children. *BMC Infect. Dis.* **14**, 569 (2014).

- 949 34. J. T. Thom, S. M. Walton, N. Torti, A. Oxenius, Salivary gland resident APCs are Flt3L- and CCR2-
950 independent macrophage-like cells incapable of cross-presentation. *Eur. J. Immunol.* **44**, 706–714
951 (2013).
- 952 35. J. T. Thom, T. C. Weber, S. M. Walton, N. Torti, A. Oxenius, The Salivary Gland Acts as a Sink for Tissue-
953 Resident Memory CD8+ T Cells, Facilitating Protection from Local Cytomegalovirus Infection.
954 *CellReports*, 1–13 (2015).
- 955 36. C. J. Smith, S. Caldeira-Dantas, H. Turula, C. M. Snyder, Murine CMV Infection Induces the Continuous
956 Production of Mucosal Resident T Cells. *CellReports*, 1–13 (2015).
- 957 37. S. M. Kallert *et al.*, Replicating viral vector platform exploits alarmin signals for potent CD8+ T cell-
958 mediated tumour immunotherapy. *Nat Commun.* **8**, 15327 (2017).
- 959 38. K. A. Hogquist *et al.*, T cell receptor antagonist peptides induce positive selection. *Cell.* **76**, 17–27
960 (1994).
- 961 39. E. M. Steinert *et al.*, Quantifying Memory CD8 T Cells Reveals Regionalization of
962 Immunosurveillance. *Cell.* **161**, 737–749 (2015).
- 963 40. X. Ficht, F. Thelen, B. Stolp, J. V. Stein, Preparation of Murine Submandibular Salivary Gland for Upright
964 Intravital Microscopy. *J Vis Exp*, 1–8 (2018).
- 965 41. D. Brändle *et al.*, T cell development and repertoire of mice expressing a single T cell receptor alpha
966 chain. *Eur J Immunol.* **25**, 2650–2655 (1995).
- 967 42. A. Marquardt *et al.*, Single cell detection of latent cytomegalovirus reactivation in host tissue. *Journal*
968 *of General Virology.* **92**, 1279–1291 (2011).
- 969 43. F. R. Stahl *et al.*, Nodular Inflammatory Foci Are Sites of T Cell Priming and Control of Murine
970 Cytomegalovirus Infection in the Neonatal Lung. *PLoS Pathog.* **9**, e1003828–18 (2013).

- 971 44. F. Ginhoux, S. Jung, Monocytes and macrophages: developmental pathways and tissue homeostasis.
972 *Nat Rev Immunol.* **14**, 392–404 (2014).
- 973 45. S. Epelman, K. J. Lavine, G. J. Randolph, Origin and Functions of Tissue Macrophages. *Immunity.* **41**,
974 21–35 (2014).
- 975 46. Y. Lavin, A. Mortha, A. Rahman, M. Merad, Regulation of macrophage development and function in
976 peripheral tissues. *Nat Rev Immunol.* **15**, 731–744 (2015).
- 977 47. A. W. Roberts *et al.*, Tissue-Resident Macrophages Are Locally Programmed for Silent Clearance of
978 Apoptotic Cells. *Immunity.* **47**, 913–927.e6 (2017).
- 979 48. S. Woyciechowski, M. Hofmann, H. Pircher, α 4 β 1 integrin promotes accumulation of tissue-resident
980 memory CD8 +T cells in salivary glands. *Eur. J. Immunol.* **47**, 244–250 (2016).
- 981 49. J. Tønnesen, V. V. G. K. Inavalli, U. V. Nägerl, Super-Resolution Imaging of the Extracellular Space in
982 Living Brain Tissue. *Cell.* **172**, 1108–1121.e15 (2018).
- 983 50. A. Le, M. Saverin, A. R. Hand, Distribution of Dendritic Cells in Normal Human Salivary Glands. *Acta*
984 *Histochem. Cytochem.* **44**, 165–173 (2011).
- 985 51. E. L. Gautier *et al.*, Gene-expression profiles and transcriptional regulatory pathways that underlie the
986 identity and diversity of mouse tissue macrophages. *Nat Immunol.* **13**, 1118–1128 (2012).
- 987 52. M. Bombardieri *et al.*, Inducible Tertiary Lymphoid Structures, Autoimmunity, and Exocrine
988 Dysfunction in a Novel Model of Salivary Gland Inflammation in C57BL/6 Mice. *J. Immunol.* **189**, 3767–
989 3776 (2012).
- 990 53. E. Russo *et al.*, Intralymphatic CCL21 Promotes Tissue Egress of Dendritic Cells through Afferent
991 Lymphatic Vessels. *CellReports.* **14**, 1723–1734 (2016).
- 992 54. G. E. Davis, The Mac-1 and p150,95 beta 2 integrins bind denatured proteins to mediate leukocyte
993 cell-substrate adhesion. *Exp Cell Res.* **200**, 242–252 (1992).

- 994 55. E. K. Paluch, I. M. Aspalter, M. Sixt, Focal Adhesion–Independent Cell Migration. *Annu. Rev. Cell Dev. Biol.* **32**, 469–490 (2016).
- 995
- 996 56. J. T. H. Mandeville, M. A. Lawson, F. R. Maxfield, Dynamic imaging of neutrophil migration in three
997 dimensions: mechanical interactions between cells and matrix. *J Leukoc Biol.* **61**, 188–200 (1997).
- 998 57. S. Nourshargh, P. L. Hordijk, M. Sixt, Breaching multiple barriers: leukocyte motility through venular
999 walls and the interstitium. *Nat Rev Mol Cell Biol.* **11**, 366–378 (2010).
- 1000 58. M. Baratin *et al.*, T Cell Zone Resident Macrophages Silently Dispose of Apoptotic Cells in the Lymph
1001 Node. *Immunity*, 1–20 (2017).
- 1002 59. S. Uderhardt, A. J. Martins, J. S. Tsang, T. Lämmermann, R. N. Germain, Resident Macrophages Cloak
1003 Tissue Microlesions to Prevent Neutrophil-Driven Inflammatory Damage. *Cell.* **177**, 541–555.e17
1004 (2019).
- 1005 60. Y. Natsuaki *et al.*, Perivascular leukocyte clusters are essential for efficient activation of effector T cells
1006 in the skin. *Nat Immunol*, 1–8 (2014).
- 1007 61. K. W. Cho *et al.*, An MHC II-Dependent Activation Loop between Adipose Tissue Macrophages and
1008 CD4+ T Cells Controls Obesity-Induced Inflammation. *CellReports.* **9**, 605–617 (2014).
- 1009 62. T. A. Wynn, A. Chawla, J. W. Pollard, Macrophage biology in development, homeostasis and disease.
1010 *Nature.* **496**, 445–455 (2013).
- 1011 63. M. Hulsmans *et al.*, Macrophages Facilitate Electrical Conduction in the Heart. *Cell.* **169**, 510–513.e20
1012 (2017).
- 1013 64. A. Scholer, S. Hugues, A. Boissonnas, L. Fetler, S. Amigorena, Intercellular adhesion molecule-1-
1014 dependent stable interactions between T cells and dendritic cells determine CD8+ T cell memory.
1015 *Immunity.* **28**, 258–270 (2008).

- 1016 65. Z. Haimon *et al.*, Re-evaluating microglia expression profiles using RiboTag and cell isolation
1017 strategies. *Nat Immunol*, 1–13 (2018).
- 1018 66. P. Mrass *et al.*, CD44 Mediates Successful Interstitial Navigation by Killer T Cells and Enables Efficient
1019 Antitumor Immunity. *Immunity*. **29**, 971–985 (2008).
- 1020 67. M. G. Overstreet *et al.*, Inflammation-induced interstitial migration of effector CD4⁺ T cells is
1021 dependent on integrin α V. *Nat Immunol*. **14**, 949–958 (2013).
- 1022 68. Y.-J. Liu *et al.*, Confinement and Low Adhesion Induce Fast Amoeboid Migration of Slow Mesenchymal
1023 Cells. *Cell*. **160**, 659–672 (2015).
- 1024 69. V. Ruprecht *et al.*, Cortical Contractility Triggers a Stochastic Switch to Fast Amoeboid Cell Motility.
1025 *Cell*. **160**, 673–685 (2015).
- 1026 70. M. Bergert *et al.*, Force transmission during adhesion-independent migration. *Nat Cell Biol*. **17**, 524–
1027 529 (2015).
- 1028 71. G. Charras, E. Sahai, Physical influences of the extracellular environment on cell migration. *Nat Rev*
1029 *Mol Cell Biol*. **15**, 813–824 (2014).
- 1030 72. K. Kendall, A. D. Roberts, van der Waals forces influencing adhesion of cells. *Philosophical Transactions*
1031 *of the Royal Society B: Biological Sciences*. **370**, 20140078–20140078 (2014).
- 1032 73. M. H. Lee, D. A. Brass, R. Morris, R. J. Composto, P. Ducheyne, The effect of non-specific interactions
1033 on cellular adhesion using model surfaces. *Biomaterials*. **26**, 1721–1730 (2005).
- 1034 74. R. J. Hawkins *et al.*, Pushing off the Walls: A Mechanism of Cell Motility in Confinement. *Phys. Rev.*
1035 *Lett*. **102**, 1567–4 (2009).
- 1036 75. T. Lämmermann *et al.*, Rapid leukocyte migration by integrin-independent flowing and squeezing.
1037 *Nature*. **453**, 51–55 (2008).

- 1038 76. K. Wolf *et al.*, Physical limits of cell migration: Control by ECM space and nuclear deformation and
1039 tuning by proteolysis and traction force. *J Cell Biol.* **201**, 1069–1084 (2013).
- 1040 77. R. G. Rowe, S. J. Weiss, Breaching the basement membrane: who, when and how? *Trends in Cell*
1041 *Biology.* **18**, 560–574 (2008).
- 1042 78. K. Wolf, Amoeboid shape change and contact guidance: T-lymphocyte crawling through fibrillar
1043 collagen is independent of matrix remodeling by MMPs and other proteases. *Blood.* **102**, 3262–3269
1044 (2003).
- 1045 79. J. Renkawitz *et al.*, Nuclear positioning facilitates amoeboid migration along the path of least
1046 resistance. *Nature.* **568**, 546–550 (2019).
- 1047 80. S. Halle *et al.*, In Vivo Killing Capacity of Cytotoxic T Cells Is Limited and Involves Dynamic Interactions
1048 and T Cell Cooperativity. *Immunity.* **44**, 233–245 (2016).
- 1049 81. B. C. Schaefer, M. L. Schaefer, J. W. Kappler, P. Marrack, R. M. Kedl, Observation of antigen-dependent
1050 CD8+ T-cell/ dendritic cell interactions in vivo. *Cell Immunol.* **214**, 110–122 (2001).
- 1051 82. A. C. Kirby, M. C. Coles, P. M. Kaye, Alveolar Macrophages Transport Pathogens to Lung Draining
1052 Lymph Nodes. *J. Immunol.* **183**, 1983–1989 (2009).
- 1053 83. A. J. Ozga *et al.*, pMHC affinity controls duration of CD8 +T cell–DC interactions and imprints timing of
1054 effector differentiation versus expansion. *J. Exp. Med.* **213**, 2811–2829 (2016).
- 1055 84. R. L. Lindquist *et al.*, Visualizing dendritic cell networks in vivo. *Nat Immunol.* **5**, 1243–1250 (2004).
- 1056 85. B. Stolp *et al.*, HIV-1 Nef interferes with T-lymphocyte circulation through confined environments in
1057 vivo. *Proceedings of the National Academy of Sciences.* **109**, 18541–18546 (2012).
- 1058 86. M. Vladymyrov, J. Abe, F. Moalli, J. V. Stein, A. Ariga, Real-time tissue offset correction system for
1059 intravital multiphoton microscopy. *Journal of Immunological Methods.* **438**, 35–41 (2016).

- 1060 87. D. C. Marshall *et al.*, Selective Allosteric Inhibition of MMP9 Is Efficacious in Preclinical Models of
1061 Ulcerative Colitis and Colorectal Cancer. *PLoS ONE*. **10**, e0127063–26 (2015).
- 1062 88. L. G. Guidotti *et al.*, Immunosurveillance of the Liver by Intravascular Effector CD8+ T Cells. *Cell*. **161**,
1063 486–500 (2015).
- 1064 89. P. Paul-Gilloteaux *et al.*, eC-CLEM: flexible multidimensional registration software for correlative
1065 microscopies. *Nat Meth*. **14**, 102–103 (2017).
- 1066

1067 **Figure legends**

1068 **Fig. 1. Dynamic motility parameters of memory CD8⁺ T cells in PLN versus SMG.** **A.** Experimental layout for
1069 CD8⁺ T cell analysis in SMG and PLN. **B.** Immunofluorescent sections of GFP⁺ OT-I T cells in PLN and SMG in
1070 memory phase (\geq day 30 p.i.). Scale bar, 100 μ m (left panels) and 20 μ m (right panel). **C.** Time-lapse 2PM
1071 image sequences showing OT-I CD8⁺ T_{PLN-M} cell motility in PLN in memory phase (\geq day 30 p.i.). **D and E.** Time-
1072 lapse 2PM image sequences showing OT-I CD8⁺ T_{RM} cell motility in SMG in memory phase (\geq day 30 p.i.).
1073 Arrowheads indicate protrusions (**D**) and the arrow indicates squeezing behavior (**E**) of OT-I CD8⁺ T_{RM}. Scale
1074 bar in C-E, 10 μ m. Time in min:s. **F.** Time-coded shapes of exemplary T_{PLN-M} and T_{RM} tracks. **G.** Shape factor
1075 distribution of T_{PLN-M} and T_{RM} with exemplary cell shapes. **H.** Speed frequency distribution of OT-I CD8⁺ T cells
1076 in PLN and SMG. Arrows indicate median values (μ m/min). **I.** Arrest coefficient frequency distribution of OT-
1077 I CD8⁺ T cells in PLN and SMG (cut-off < 2.5 μ m/min). **J.** Mean displacement versus time of OT-I T_{PLN-M} (left)
1078 and T_{RM} (right) before and after OVA₂₅₇₋₂₆₄ injection with motility coefficients (μ m²/min). **K.** IFN- γ expression
1079 in OT-I T_{PLN-M} and T_{RM} 24 h after OVA₂₅₇₋₂₆₄ injection (mean \pm SD). **L, M.** Speeds (L) and meandering index (M)
1080 of P14 CD8⁺ T cells in PLN and SMG in memory phase (\geq day 30 p.i.) of LCMV Armstrong infection. **N.** Speeds
1081 of P14 CD8⁺ T cells SMG T_{RM} cells after injection of irrelevant (OVA₂₅₇₋₂₆₄) or cognate (gp₃₃₋₄₁) peptide. Red
1082 lines indicate median. **O.** Speeds of OT-I CD8⁺ T_{RM} cells in LG in memory phase (\geq day 30 p.i.) after LCMV-OVA
1083 infection. Data in G are from 2-3 independent experiments and 3 mice total for each group. Data in H and I
1084 are pooled from 5 to 6 mice from 4 independent experiments with at least 194 tracks analyzed per organ.
1085 Data in J are pooled of 3-4 mice from 2 independent experiments. Data in K show one of two independent
1086 experiments. Data in L and M are from 4-7 mice and in N from 1-4 mice in 1-3 independent experiments.
1087 Data in G, I and M were analyzed with Mann-Whitney-test and data in H, L and N with Student's t-test. ***,
1088 $p < 0.001$.

1089

1090 **Fig. 2. T_{RM} colocalize with tissue macrophages in SMG and LG.** **A.** Immunofluorescent section showing
1091 localization of SMG T_{RM} adjacent to tissue macrophages (arrows). Scale bars, 1 mm (left), 100 μ m (middle)
1092 and 20 μ m (right). **B.** Percent of SMG T_{RM} adjacent to tissue macrophages. Data are pooled from 105 FOV
1093 with a total of 3270 T_{RM} and shown as box and whisker graph with 2.5 – 97.5 percentiles. **C.**

1094 Immunofluorescent LG section in memory phase (≥ 30 days p.i. with LCMV-OVA) showing GFP⁺ OT-I T_{RM}
1095 adjacent to CD11c-YFP⁺ tissue macrophages (indicated by yellow arrowheads). Scale bars, 1 mm (left), 100
1096 μm (middle) and 20 μm (right). **D.** Correlative light and electron microscopy sections (left; confocal image;
1097 middle and right, TEM image) showing close spatial association of SMG T_{RM} and tissue macrophages. M, tissue
1098 macrophages; E, epithelial cell; ME, myoepithelial cell; ECM, extracellular matrix. Scale bar, 5 (left), 2 (middle)
1099 and 1 μm (right). **E.** TEM images showing attachment of epithelial cells to ECM (top) and through intercellular
1100 junctions (white arrows; bottom). Scale bar, 800 nm. **F.** Immunofluorescent section of WT and CXCR3^{-/-} OT-I
1101 T cells and macrophages. Magnified image shows association of CXCR3^{-/-} OT-I T_{RM} to tissue macrophages
1102 (arrows). Scale bar, 100 μm (left) and 20 μm (right). **G.** Dispersed T cells (brown) in human parotid salivary
1103 gland associate with macrophage cell bodies or thin protrusions (red), indicated by arrowheads. Scale bar,
1104 20 μm . **H.** Example of colocalization of CD68⁺ macrophage (red) and CD3⁺ T cell clusters (brown) in human
1105 parotid salivary gland. Scale bar, 50 μm .

1106

1107 **Fig. 3. Macrophage depletion disrupts T_{RM} patrolling.** **A.** 2PM time-lapse image sequence showing overlap
1108 of OT-I T_{RM} tracks with tissue macrophages in SMG in memory phase (\geq day 30 p.i.). Scale bar, 20 μm . Time
1109 in min:s. The right panels show the time accumulated overlays of images with or without OT-I T_{RM}. **B.** 2PM
1110 time-lapse image sequence of T_{RM} in DTx-treated CD11c-YFP or CD11c-DTR -> Ubi-GFP chimeras. Magenta
1111 lines indicate outlines of acini, white segmented lines indicate cell tracks. Scale bar, 50 μm (overview) and 20
1112 μm (insert). Time in min:s. **C.** Example T_{RM} tracks in presence or absence of macrophage. Scale bar, 10 μm .
1113 **D.** Frequency distribution of T_{RM} speeds in DTx-treated CD11c-YFP or CD11c-DTR bone marrow chimera.
1114 Arrows indicate median ($\mu\text{m}/\text{min}$). Data are pooled from 2-4 independent experiments with 4-6 mice total
1115 and analyzed with Mann-Whitney test; ***, $p < 0.001$. **E.** Track analysis outline. Top panel. U-turns (red)
1116 describe tracks reversing direction while excluding continuous turns. Bottom panel. Synthetic tracks were
1117 generated to assess dwell time in an 80 μm -diameter sphere (black). One example track is shown for control
1118 (light blue) and macrophage-depleted (dark blue) condition. **F.** Percent of tracks making U-turn. Bars indicate
1119 95% confidence intervals. **G.** *In silico* dwell times for T_{RM} tracks in 80 μm -spheres based on measured track
1120 parameters.

1121

1122 **Fig. 4. Absence of macrophages reduces T_{RM} movement into and out of epithelium. A and B.** 2PM time-
1123 lapse image sequences of T_{RM} crawling along a macrophage to enter acini in UbiGFP (A) and mT/mG (B) bone
1124 marrow recipients. Epithelial signal was manually masked to show an isolated acinus in zoomed panels.
1125 Dashed white line indicates area displayed in xz-view, and arrow indicates T_{RM} - macrophage contact. A. Scale
1126 bar, 50 μm (overview) and 20 μm (insert); B. Scale bar, 20 μm (overview) and 10 μm (insert). Time in min:s.
1127 **C.** Percentage of T_{RM} transitions into or out of acini and ducts in CD11c-YFP -> Ubi-GFP chimeras (n = 42) with
1128 and without contact to macrophages. **D and E.** 2PM time-lapse image sequence of CD11cYFP -> Ubi-GFP and
1129 DTx-treated CD11cDTR->Ubi-GFP chimeras were analyzed for T_{RM} crossing events (leaving or entering acini).
1130 D shows average transitions per hour track duration, and E depicts transitions per 1000 μm total distance
1131 migrated. Data points represent individual image sequences. Line indicates mean. **F.** Experimental layout for
1132 analysis of T_{RM} response to local chemokine. CXCL10 was injected with a fluorescent tracer (Qdots₆₅₅) for 4 h
1133 to allow T_{RM} accumulation. Integrin blocking mAbs prevent recruitment of circulating T cells. **G.** T_{RM} per cm^2
1134 at sites of CXCL10 injection in presence or absence of macrophages. Numbers indicate mean \pm SD. Data in D
1135 and F are pooled from 2-4 independent experiments with 4-6 mice total. Data in D was analyzed with Mann-
1136 Whitney and data in F was analyzed with Wilcoxon rank test. *, p < 0.05.

1137

1138 **Fig. 5. SMG macrophages show discontinuous attachment to neighboring cells. A.** Confocal SMG section
1139 showing pTyr signal in tissue macrophages. Left panel shows macrophage/pTyr/DAPI signal, right panels
1140 show three consecutive z-stacks (spacing 1 μm) of macrophage/pTyr signal. Scale bar, 3 μm . **B.** Quantification
1141 of pTyr⁺ protrusions. **C.** Experimental layout of super-resolution shadow imaging (SUSHI) of SMG slices. **D.**
1142 Example of SUSHI image for determination of extracellular space. E, epithelium; BV, blood vessel. Scale bar,
1143 10 μm . **E.** Overview of ECS signal with SMG epithelium (E) and CD11c-YFP⁺ tissue macrophages. Scale bar, 10
1144 μm . **F.** Example of epithelial attachment before and after hyperosmotic challenge. Arrows show
1145 interepithelial junctions. Scale bar, 5 μm . **G.** Examples of macrophage detachment before and after
1146 hyperosmotic challenge. Arrowheads indicate detachment. Scale bar, 5 μm . **H.** Quantification of gap size
1147 between macrophage and epithelium before and after hyperosmotic challenge. **I.** Confocal image of SMG

1148 section with macrophage protrusions traversing a basement membrane below an epithelial acinus (indicated
1149 by arrow). Scale bar, 20 μm (overview) and 5 μm (insert). **J.** Electron microscopy image of macrophages
1150 creating a discontinuation of the basement membrane of an acinus (indicated by arrow). Numbers mark two
1151 neighboring macrophages. Arrowheads indicate lack of tight adhesion between macrophages and
1152 neighboring cells. Scale bar, 2 μm . All images are representative of at least 2 independent experiments. Data
1153 in H were analyzed using a paired t-test. ***, $p < 0.001$.

1154

1155 **Fig. 6. Robust *in vivo* SMG T_{RM} motility after inhibition of $G\alpha_i$ and integrins.** **A.** Experimental layout. **B.** OT-I
1156 $T_{\text{PLN-M}}$ and T_{RM} speeds after combined anti- α_L , α_4 and α_E integrin mAb (αltg) inhibition. Arrows indicate
1157 median values ($\mu\text{m}/\text{min}$). **C.** 2PM image of T_{RM} – tissue macrophage colocalization in αltg -treated SMG.
1158 Arrows indicate T cell – tissue macrophage contacts. Scale bar, 20 μm . **D.** OT-I T_{RM} speeds in SMG after WD
1159 administration of RAD or RGD peptide. **E.** WT and $\text{CXCR3}^{-/-}$ OT-I T_{RM} speeds in SMG in memory phase (\geq day
1160 30 p.i.). Arrows indicate median values ($\mu\text{m}/\text{min}$). **F.** OT-I $T_{\text{PLN-M}}$ and T_{RM} speeds after systemic treatment with
1161 active PTx or inactive (mutant) PTx (PTx_{mut}). Arrows indicate median values ($\mu\text{m}/\text{min}$). **G.** 2PM image of T_{RM} –
1162 tissue macrophage colocalization in PTx-treated SMG. Arrows indicate T cell – tissue macrophage contacts.
1163 Scale bar, 20 μm . **H.** Flow cytometry plot of mixed T_{RM} and macrophages. **I.** Quantification of cluster formation
1164 as shown in H. Data in B, D, E and F are pooled from 2-5 independent experiments with a total of 2-7 mice
1165 with at least 111 tracks per condition and analyzed with unpaired Student's t-test. Data in I are pooled from
1166 2 independent experiments and analyzed using unpaired Student's t-test. ***, $p < 0.001$.

1167

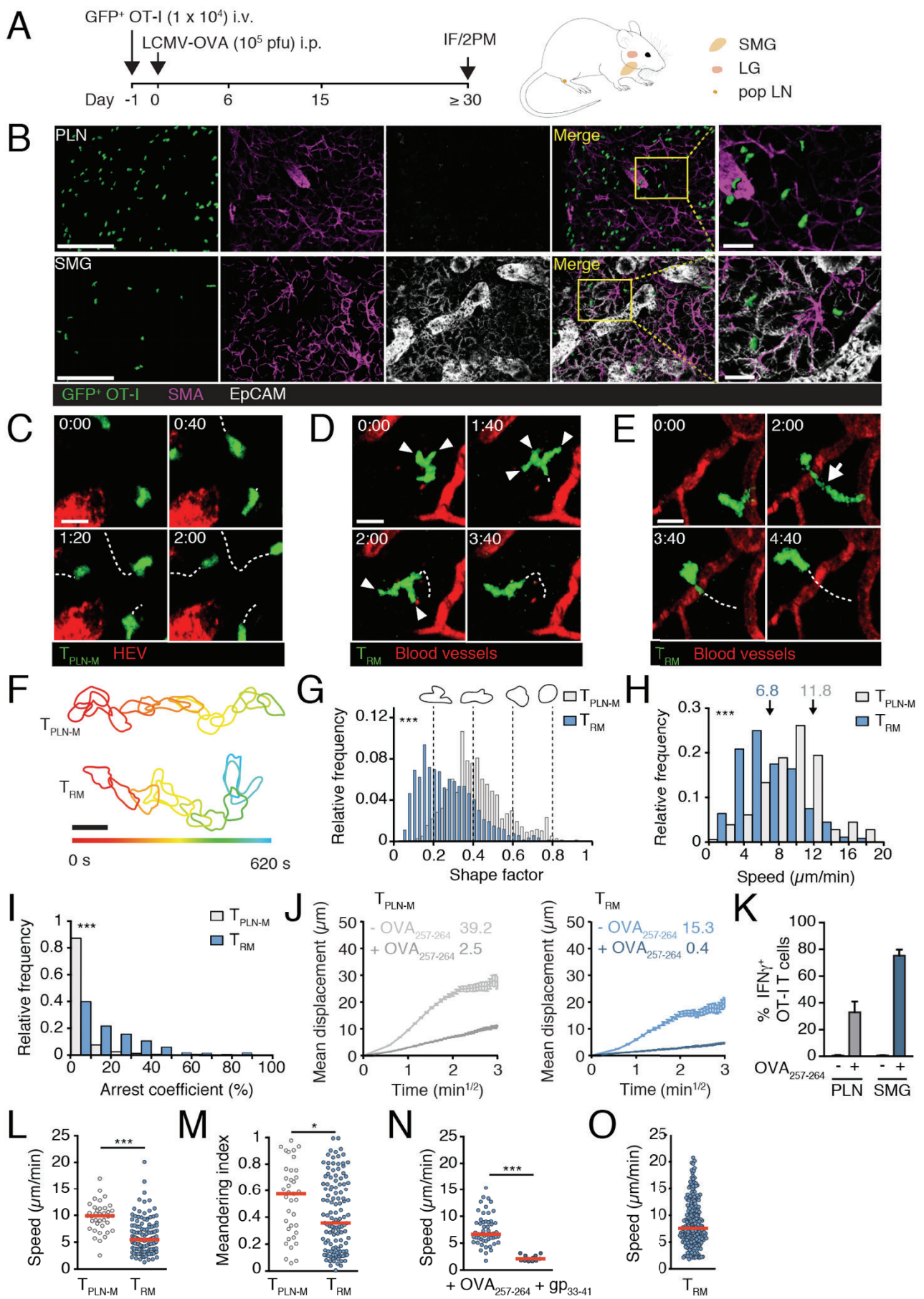
1168 **Fig. 7. Confinement induces autonomous SMG T_{RM} motility through friction.** **A.** Experimental layout of under
1169 agarose assay. Arrows indicate F-actin flow. **B.** Representative T_{N} ($n = 75$) and T_{RM} ($n = 58$) tracks in presence
1170 of chemokine and ICAM-1. **C.** Speeds of T_{N} and T_{RM} . Data are presented as Tukey box and whiskers plot. **D.**
1171 Time-lapse image sequence showing T_{RM} motility among immotile T_{N} . T_{RM} displacement shown by segmented
1172 line. Scale bar, 20 μm . Time in min:s. **E.** Time-lapse image sequence in under agarose plates coated with HSA
1173 showing $T_{\text{PLN-M}}$ (top) and T_{RM} (bottom) motility. Cell displacement shown by segmented line. Scale bar, 10 μm .
1174 Time in min:s. **F.** Representative T_{N} ($n = 75$), $T_{\text{PLN-M}}$ ($n = 226$) and T_{RM} ($n = 379$) tracks. **G.** T_{N} , $T_{\text{PLN-M}}$ and T_{RM}

1175 speeds in under agarose plates coated with HSA. Numbers indicate percentage of tracks $> 3 \mu\text{m}/\text{min}$ (boxed).
1176 Lines indicate median. **H.** Meandering index of T_N , $T_{\text{PLN-M}}$ and T_{RM} tracks. **I.** Example image sequences showing
1177 T_{RM} in transient contact with macrophages under agarose on fibronectin-coated plates. T_{RM} displacement is
1178 shown by segmented line. Scale bar, $50 \mu\text{m}$. Time in min:s. **J.** T_{RM} – macrophage contact duration for individual
1179 tracks. **K.** Time-lapse image sequence showing SMG (green) epidermal T_{RM} (red) under agarose on HSA. SMG
1180 T_{RM} displacement shown by segmented line. Scale bar, $20 \mu\text{m}$. Time in min:s. **L.** Speeds of SMG and epidermal
1181 T_{RM} in under agarose plates coated with HSA. **M.** T_{RM} speeds after treatment with PTx, RGD peptide, anti-
1182 Mac1 mAb, or in presence of EDTA. Numbers indicate percentage of tracks $> 3 \mu\text{m}/\text{min}$ (boxed). Lines indicate
1183 median, dotted line represents median speed of control. **N.** Image sequence of T_{RM} protrusions in presence
1184 of EDTA. Scale bar, $10 \mu\text{m}$. **O.** Representative T_{RM} cell tracks in presence of EDTA ($n = 75$). **P.** Mean
1185 displacement over time of T_{RM} tracks. Numbers indicate motility coefficients ($\mu\text{m}^2/\text{min}$). Data in C, G, H, M
1186 and P were pooled from at least 2 independent experiments each. Statistical analysis was performed with
1187 unpaired t-test (C) or Kruskal-Wallis with Dunn’s multiple comparison in G,H and M (as compared to “ T_{RM} ”).
1188 **, $p < 0.01$; ***, $p < 0.001$.

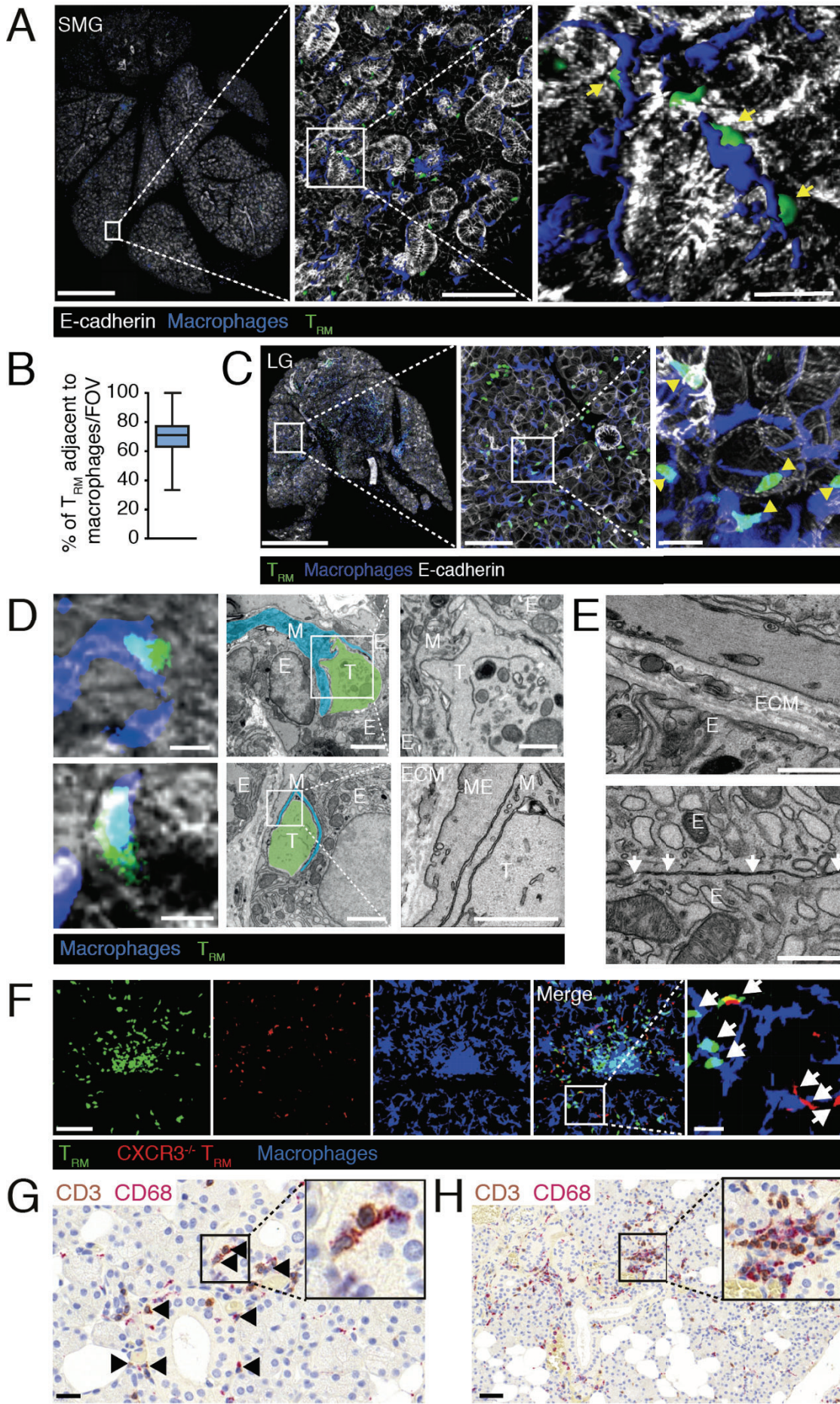
1189

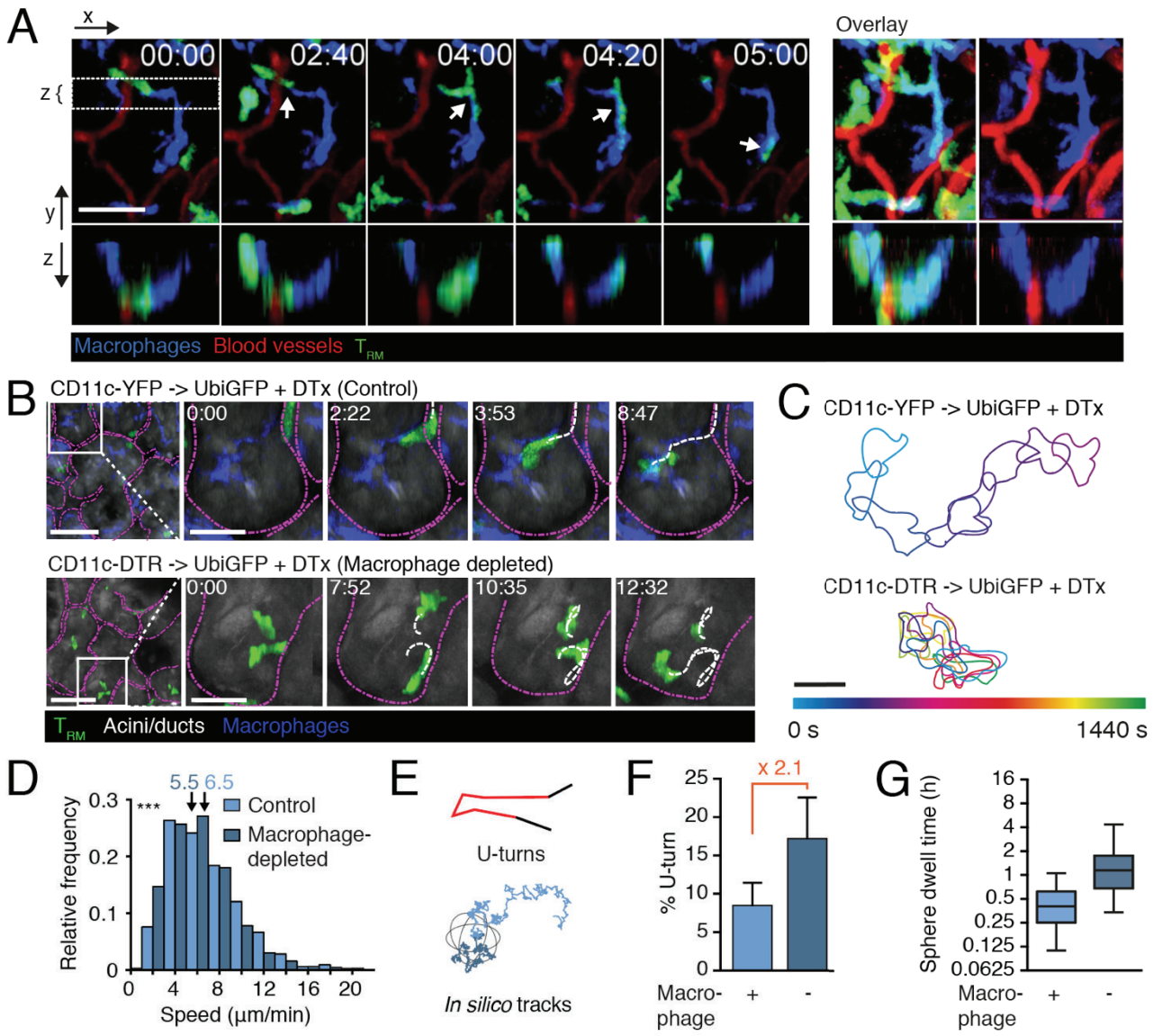
1190 **Fig. 8. T_{RM} insert protrusions for cell displacement in absence of external chemoattractants and friction. A.**
1191 Experimental layout. Arrows indicate protrusion direction. **B.** Image sequences of T_{RM} within T_N clusters in
1192 presence of EDTA. Arrowheads show membrane protrusions; segmented line indicates cell track. Scale bar,
1193 $10 \mu\text{m}$. Time in min:s. **C.** Graphical representation of T_{RM} inside T_N cluster (i) or dispersed (ii). **D.** T_{RM} track
1194 speeds according to their location. Numbers indicate percentage of tracks $> 3 \mu\text{m}/\text{min}$ (boxed). Lines indicate
1195 median. **E.** Meandering index of T_{RM} tracks sorted according to their location. Lines indicate median. **F.** Image
1196 sequences of T_{RM} alone (top) and with $7 \mu\text{m}$ polystyrene beads (bottom) in presence of EDTA. Arrowheads
1197 show membrane protrusions. Segmented line indicates cell track. Scale bar, $10 \mu\text{m}$, time in min:s. **G.** T_{RM} track
1198 speeds according to their association with or without beads. Numbers indicate percentage of tracks > 3
1199 $\mu\text{m}/\text{min}$ (boxed). Lines indicate median. **H.** Meandering index of T_{RM} tracks sorted according to their location.
1200 **I and J.** Proposed model of tissue macrophage-assisted T_{RM} immune surveillance in SMG. **I.** Confined SMG
1201 T_{RM} display distinct migration modes. *Ex vivo* confined SMG T_{RM} respond to chemoattractants and adhesion

1202 molecules, while displaying autonomous motility through friction. Furthermore, SMG T_{RM} adapt to
1203 environmental topology to insert protrusions and move between adjacent structures that are not tightly
1204 connected. J. By associating with protrusion-forming tissue macrophages, which lack extensive contacts with
1205 surrounding tissue cells, T_{RM} exploit their distinct motility modes for organ surveillance. Arrows indicate
1206 protrusion direction. E, epithelium; M, tissue macrophage. Lines indicate median. Data in D, E, G and H are
1207 pooled from 4 - 5 independent experiments. Statistical analysis was performed with Mann-Whitney test. ***,
1208 $p < 0.001$.



1209 Figure 1





1211 Figure 3

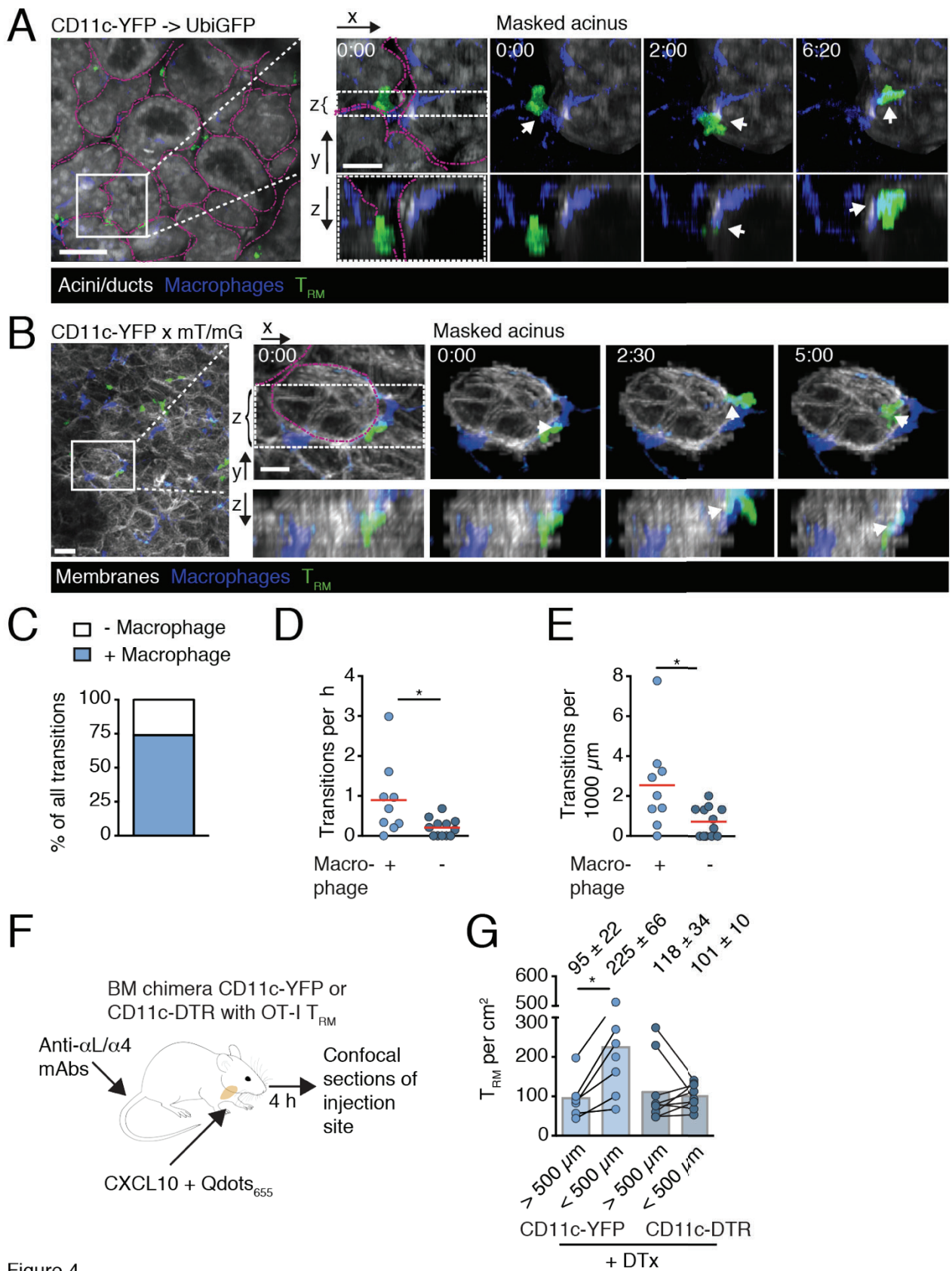
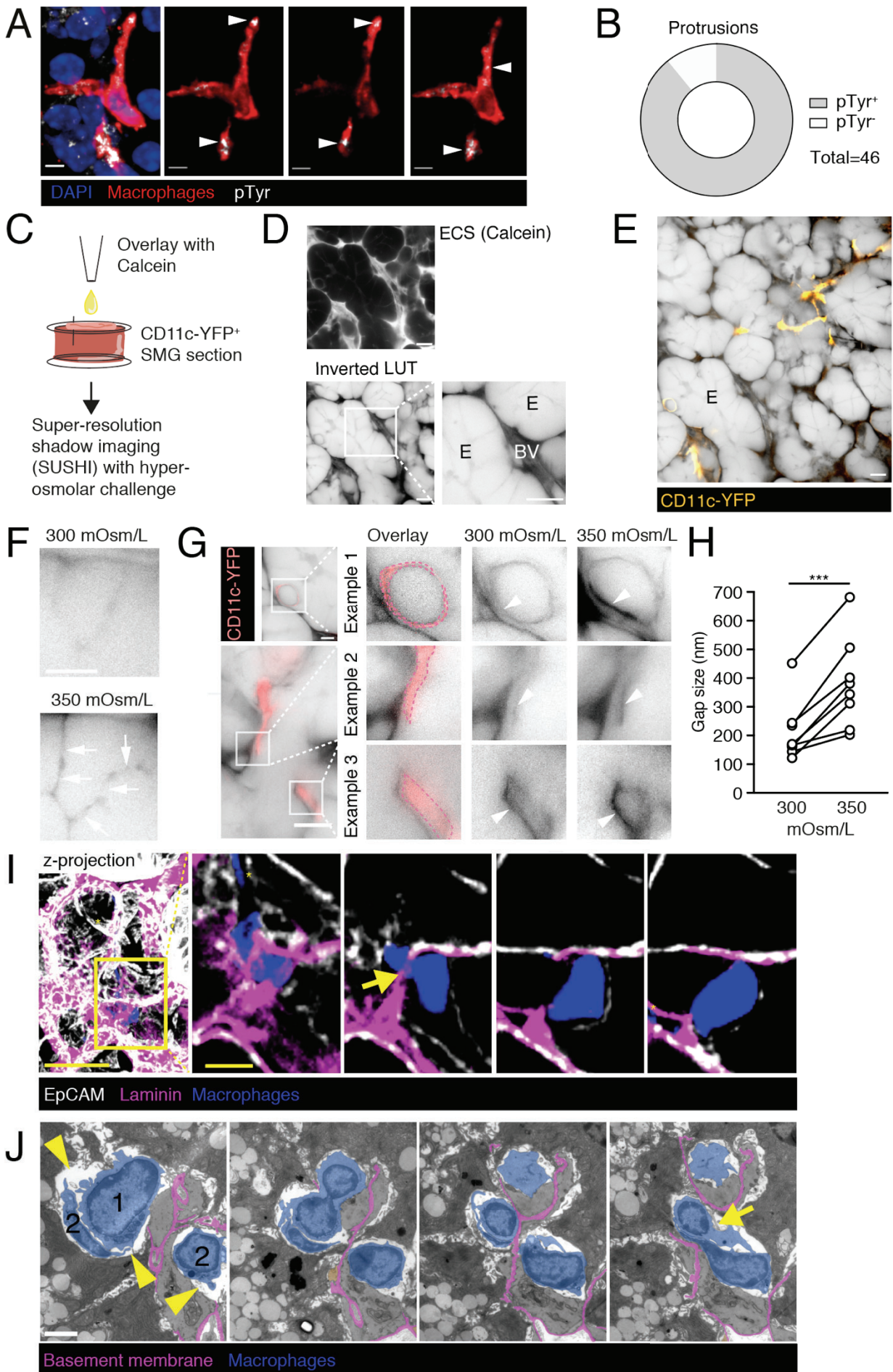


Figure 4



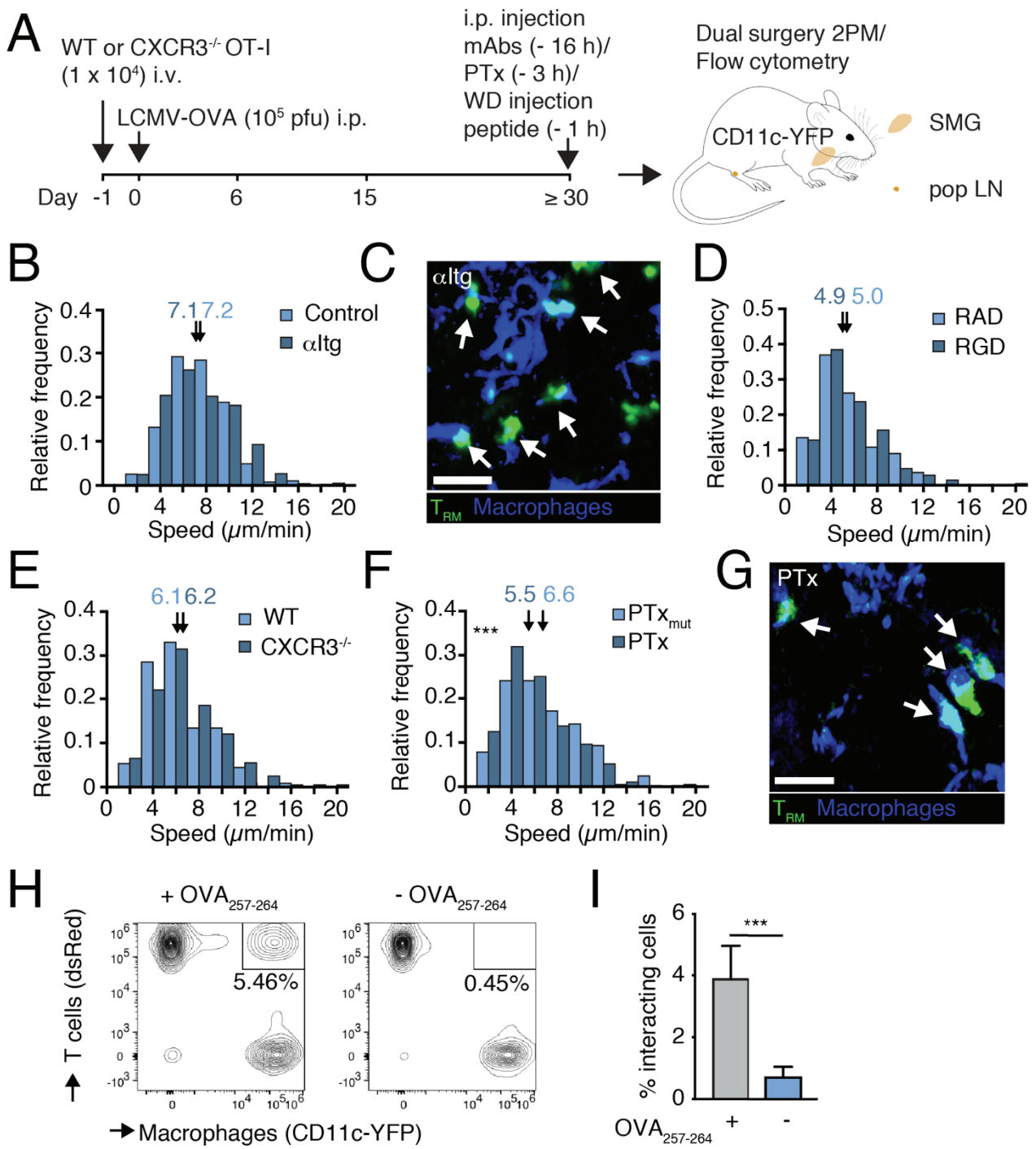


Figure 6

1214

1215

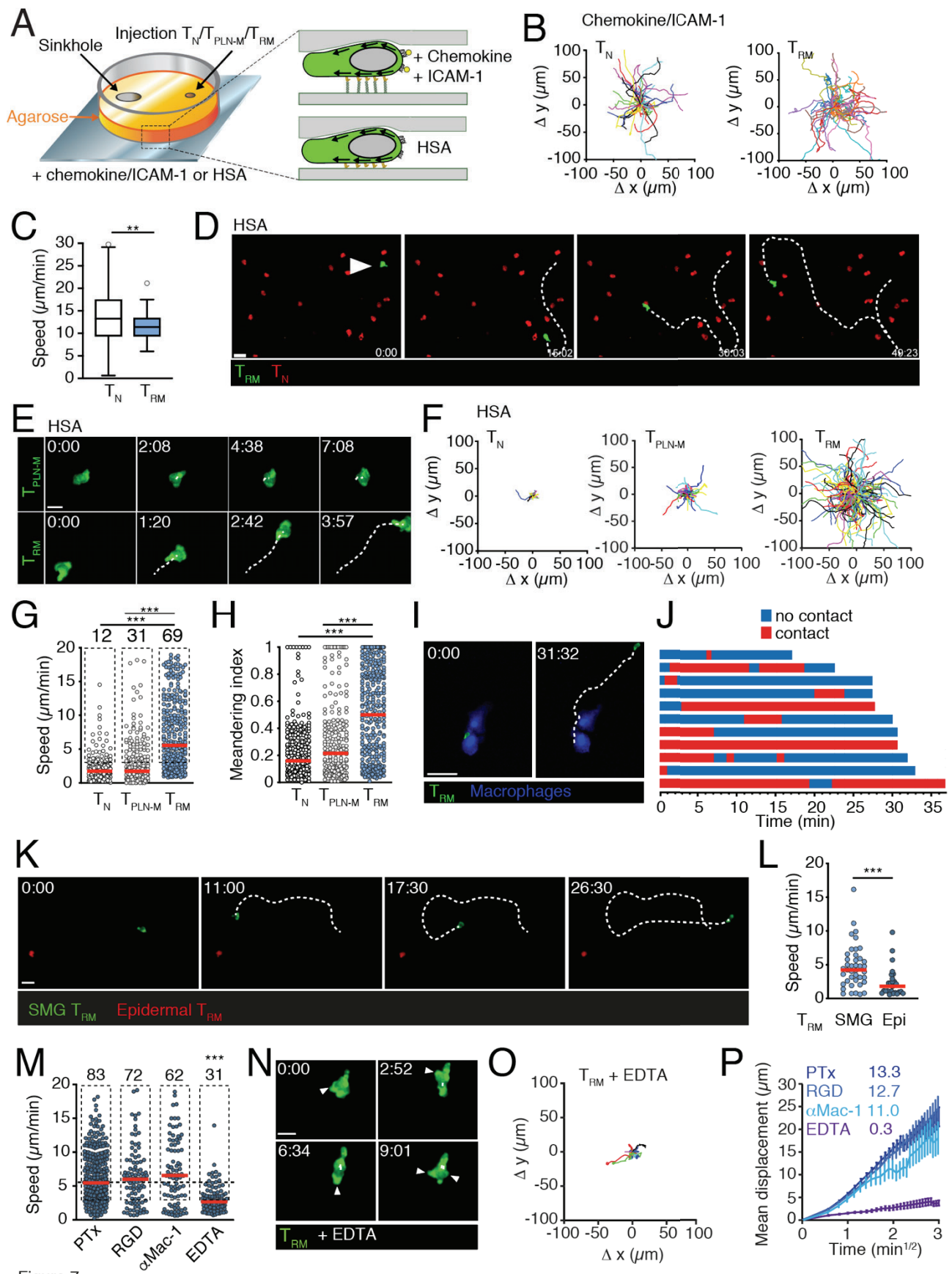


Figure 7

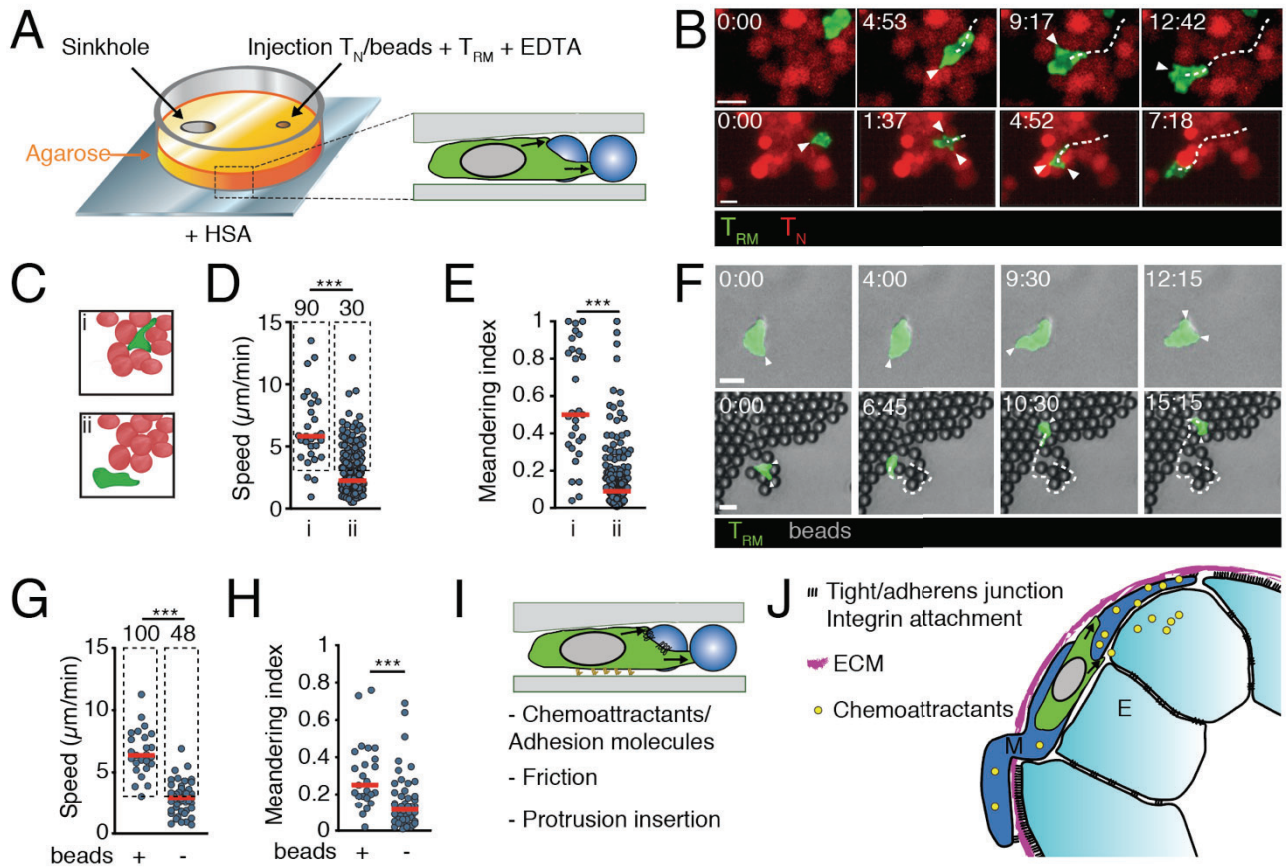


Figure 8

1217

1218

1219 **Supplementary Figures**

1220 **Figure S1. Systemic viral infection leads to memory CD8⁺ T cell populations in secondary lymphoid organs**

1221 **and SMG for comparative analysis. A.** Experimental setup to study CD8⁺ T cell behavior and phenotype in

1222 SMG and secondary lymphoid organs. GFP⁺ OT-I CD8⁺ T cells were i.v. injected on day -1. Recipient mice were

1223 infected with LCMV-OVA on day 0 and analyzed for viral titer determination and flow cytometry on indicated

1224 days. **B.** Viral titer determination on days 3 and 5 p.i. with LCMV-OVA. Each dot represents one mouse, lines

1225 indicate median. **C.** Representative flow cytometry analysis of adoptively transferred GFP⁺ OT-I T cells after

1226 gating on FSC/SSC-H lymphocyte CD45⁺ singlets. Numbers indicate percentages. **D.** Total and OT-I T cell

1227 numbers in spleen PLN and SMG at indicated days p.i. with LCMV-OVA. Each dot represents one mouse, lines

1228 indicate median. **E.** Surface marker expression on transferred OT-I T cells at indicated time points. Dotted

1229 lines are isotype or FMO (for CD69) controls. **F.** Quantification of cell surface marker expression. Plotted are

1230 mean \pm SD. Data in B are from 2 independent experiments with a total of 5-10 mice per time point. Data in F

1231 are pooled from 3-4 independent experiments with a total of 6 to 15 mice per time point, except CD69 data

1232 showing 1 of 2 independent experiments with 3 mice/time point.

1233

1234 **Figure S2. Characterization of CD11c-YFP⁺ macrophages. A.** Flow cytometry of SMG from CD11c-YFP mice.

1235 The green line represents the FMO control. Numbers indicate percentage using FMO as control. **B.**

1236 Immunofluorescent SMG section of CD11c-YFP⁺ signal and Iba-1. Iba-1⁺ CD11c-YFP⁺ cells are marked by white

1237 arrows. Scale bar, 50 μ m. **C.** Immunofluorescent SMG section showing tissue macrophages close to EpCAM⁺

1238 secretory epithelium (arrow) and SMA⁺ interstitial vasculature (arrowhead). Scale bar, 40 μ m. **D.**

1239 Immunofluorescent SMG section showing macrophages and epithelial cells in acini and ducts (identified by

1240 luminal ZO-1 labelling). Yellow dashed lines indicate outlines of acini and ducts. Scale bar, 10 μ m.

1241

1242 **Figure S3. LG T_{RM} motility parameters after macrophage depletion. A.** Frequency distribution of T_{RM} speeds

1243 in DTx-treated CD11c-YFP or CD11c-DTR bone marrow chimera (control and macrophage-depleted,

1244 respectively). Arrows indicate median (μ m/min). **B.** Percent of tracks making U-turn. Bars indicate 95%

1245 confidence intervals. Data are pooled from 2-3 independent experiments with 5 mice each and analyzed by

1246 unpaired t-test (A). ***, $p < 0.001$. **C.** In silico dwell times for T_{RM} tracks in 80 μm -spheres based on measured
1247 track parameters.

1248

1249 **Figure S4. Tissue macrophage-mediated efferocytosis during viral infection of SMG.** **A.** Experimental layout
1250 for local infection of the SMG via retrograde WD injection. **B.** Immunofluorescent SMG sections at 48 h post
1251 WD injection with MCMV-OVAmCherry. Infection is restricted to the SMG. Scale bar, 50 μm . **C.** T_{RM} and tissue
1252 macrophages cluster around infected cells. Scale bar, 50 μm . **D.** Macrophage engulfing infected cell (arrow).
1253 Scale bar, 20 μm . **E.** Quantification of mCherry⁺ foci per FOV in SMG sections 48h after MCMV-OVAmCherry
1254 infection in the presence or absence of macrophages and T_{RM} . **F.** Intensity of mCherry signal per spot in the
1255 presence or absence of T_{RM} in macrophage-depleted SMG. Data in E were analyzed with Kruskal-Wallis and
1256 Dunn's multiple comparisons test and in F with Student's unpaired t-test. ***, $p < 0.001$.

1257

1258 **Figure S5. Analysis of integrins and T_{PLN-M} blockade *in vivo*.** **A.** Expression of integrins on memory phase OT-
1259 I T cells in spleen, PLN and SMG. **B.** mAb saturation testing. Immediately after 2PM recording, PLN and SMG
1260 single cells suspensions were either incubated with the same blocking mAb, followed by a Cy5-labeled Ab
1261 against the first mAb (1st and 2nd Ab), or just with the Cy5-labeled 2^{ndary} Ab (2nd Ab only) and analyzed by flow
1262 cytometry. **C.** Frequency distribution of T_{PLN-M} speeds after integrin blockade. Arrows indicate median
1263 ($\mu\text{m}/\text{min}$). **D.** Confocal image of $\beta 1$ staining of SMG section. Arrowhead indicates macrophage - T_{RM} interface.
1264 Scale bar, 4 μm **E.** Confocal image of E-cadherin staining of SMG section. Scale bar, 5 μm . **F.** Frequency
1265 distribution of T_{PLN-M} speeds after PTx treatment. Arrows indicate median ($\mu\text{m}/\text{min}$). Data in C and F are
1266 pooled from 2-5 independent experiments with a total of 2-7 mice and analyzed with unpaired Student's t-
1267 test. ***, $p < 0.001$.

1268 **Supplementary movie Legends**

1269 **Movie S1. Intravital imaging of $T_{\text{PLN-M}}$ migration in PLN.** $T_{\text{PLN-M}}$ (green) display amoeboid shapes while
1270 migrating in the T cell zone of PLN close to HEV (red). Scale bar, 20 μm and 10 μm (zoom). Time in min:s.

1271

1272 **Movie S2. Intravital imaging of T_{RM} migration in SMG.** T_{RM} (green) migrate in the SMG between blood vessels
1273 (red). T_{RM} frequently display multiple leading edges or shape changes. Scale bar, 20 μm and 10 μm (zoom).
1274 Time in min:s.

1275

1276 **Movie S3. Confocal image of SMG T_{RM} colocalization with tissue macrophages.** T_{RM} (green) are in close
1277 proximity to tissue macrophages (blue). EpCAM-1 (white) depicts epithelial cells. Close up shows a T_{RM} in a
1278 duct, identified by ZO-1 staining (red).

1279

1280 **Movie S4. Intravital imaging of SMG T_{RM} migration along tissue resident macrophages.** Time series (left)
1281 and time accumulated overlay (right), including xy and xz projections. T_{RM} (green) frequently move along thin
1282 protrusions of CD11c⁺ tissue resident macrophages (blue). Blood vessels are shown in red. Major ticks 50 μm
1283 and 20 μm (zoom). Time in min:s.

1284

1285 **Movie S5. Intravital imaging of T_{RM} migration in the absence of macrophages.** T_{RM} (green) show migration
1286 in the absence of macrophages but are mostly confined to individual acini and ducts. Stroma is white, and
1287 outlines of acini and ducts are indicated in magenta. Time in min:s.

1288

1289 **Movie S6. Intravital imaging of T_{RM} migrate along a macrophage to enter acini.** T_{RM} (green) migrating along
1290 a macrophage (blue) to enter an acinus. Stroma is white, and outlines of acini and ducts are indicated in
1291 magenta. T_{RM} entering the acinus is indicated with an arrowhead. Second half of the Supplementary Video
1292 shows the image sequence in 3D. For better visibility, one acinus has been masked manually. Time in min:s.

1293

1294 **Movie S7. Intravital imaging of T_{RM} migration in the absence of macrophages after 5 days of DTx treatment.**

1295 T_{RM} (green) show migration in the absence of macrophages but are confined to individual acini and ducts
1296 (white). Time in min:s.

1297

1298 **Movie S8. Time-lapse SUSHI of SMG section during hyperosmotic challenge.** Extracellular space (black) at
1299 time point "0:00" depicts image before starting at "0:20" with gradual increase of osmolarity to 350 mOsm/L.
1300 During challenge, ECS increases, in particular in interstitium. Scale bar, 10 μm. Time in h:min.

1301

1302 **Movie S9. Confocal image of tissue macrophage protrusions and basement membranes in SMG.** T_{RM} (green)
1303 are in close proximity to tissue macrophages (blue). EpCAM-1 (white) depicts epithelial cells. Close up shows
1304 a tissue macrophage protruding between basement membranes labeled by laminin (magenta).

1305

1306 **Movie S10. Intravital imaging of T_{RM} migration and association with macrophages after blocking of αL, α4
1307 and αE integrins.** T_{RM} (green) move rapidly and associate with macrophages (blue) 16 h after treatment with
1308 integrin-blocking mAbs. Blood vessels are shown in red. Scale bar, 20 μm and 10 μm (zoom). Time in min:s.

1309

1310 **Movie S11. Intravital imaging of T_{RM} migration and association with macrophages after treatment with PTx.**

1311 T_{RM} (green) move rapidly and associate with macrophages (blue) 3 h after treatment with PTx. Scale bar, 20
1312 μm and 10 μm (zoom). Time in min:s.

1313

1314 **Movie S12. Time-lapse imaging of T_N migration under *in vitro* confinement on CCL21/ICAM-1-coated plates.**

1315 T_N (red) show efficient migration on CCL21/ICAM-1-coated glass slides under agarose. Scale bar, 50 μm. Time
1316 in min:s.

1317

1318 **Movie S13. Time-lapse imaging of T_{RM} migration under *in vitro* confinement on CXL10 + CXCL12/ICAM-1-
1319 coated plates.** T_{RM} (green) show efficient migration on chemokine/ICAM-1-coated glass slides under agarose.

1320 Scale bar, 20 μm. Time in min:s.

1321

1322 **Movie S14. Time-lapse imaging of T_{RM} and T_N migration under *in vitro* confinement on HSA-coated plates.**

1323 T_{RM} (green) but not T_N (red) show efficient migration on HSA-coated glass slides under agarose. Scale bar, 50
1324 μm . Time in min:s.

1325

1326 **Movie S15. Time-lapse imaging of T_{RM} and T_{PLN-M} migration under *in vitro* confinement.** T_{RM} (left) but not

1327 T_{PLN-M} (right) show efficient migration on HSA-coated glass slides under agarose. Major ticks 20 μm . Time in
1328 min:s.

1329

1330 **Movie S16. High temporal resolution analysis of T_{RM} motility under *in vitro* confinement.** T_{RM} migration on

1331 HSA-coated glass slides under agarose. Scale bar, 10 μm . Time in min:s.

1332

1333 **Movie S17. Time-lapse imaging of T_{RM} and tissue macrophages under *in vitro* confinement.** T_{RM} (green)

1334 detaching from SMG macrophages (blue) under agarose. Scale bar, 50 μm . Time in min:s.

1335

1336 **Movie S18. Time-lapse imaging of SMG and epidermal T_{RM} under *in vitro* confinement.** SMG T_{RM} (green)

1337 and epidermal T_{RM} (red) under agarose. Scale bar, 20 μm . Time in min:s.

1338

1339 **Movie S19. Time-lapse imaging of T_{RM} migration in presence of EDTA.** Left panel. T_{RM} form protrusions but

1340 do not translocate under agarose in the presence of EDTA. Right panel. T_{RM} migration is restored within

1341 clusters of T_N (red), which serve as scaffold for T_{RM} motility. Major ticks 5 μm . Time in min:s.

1342

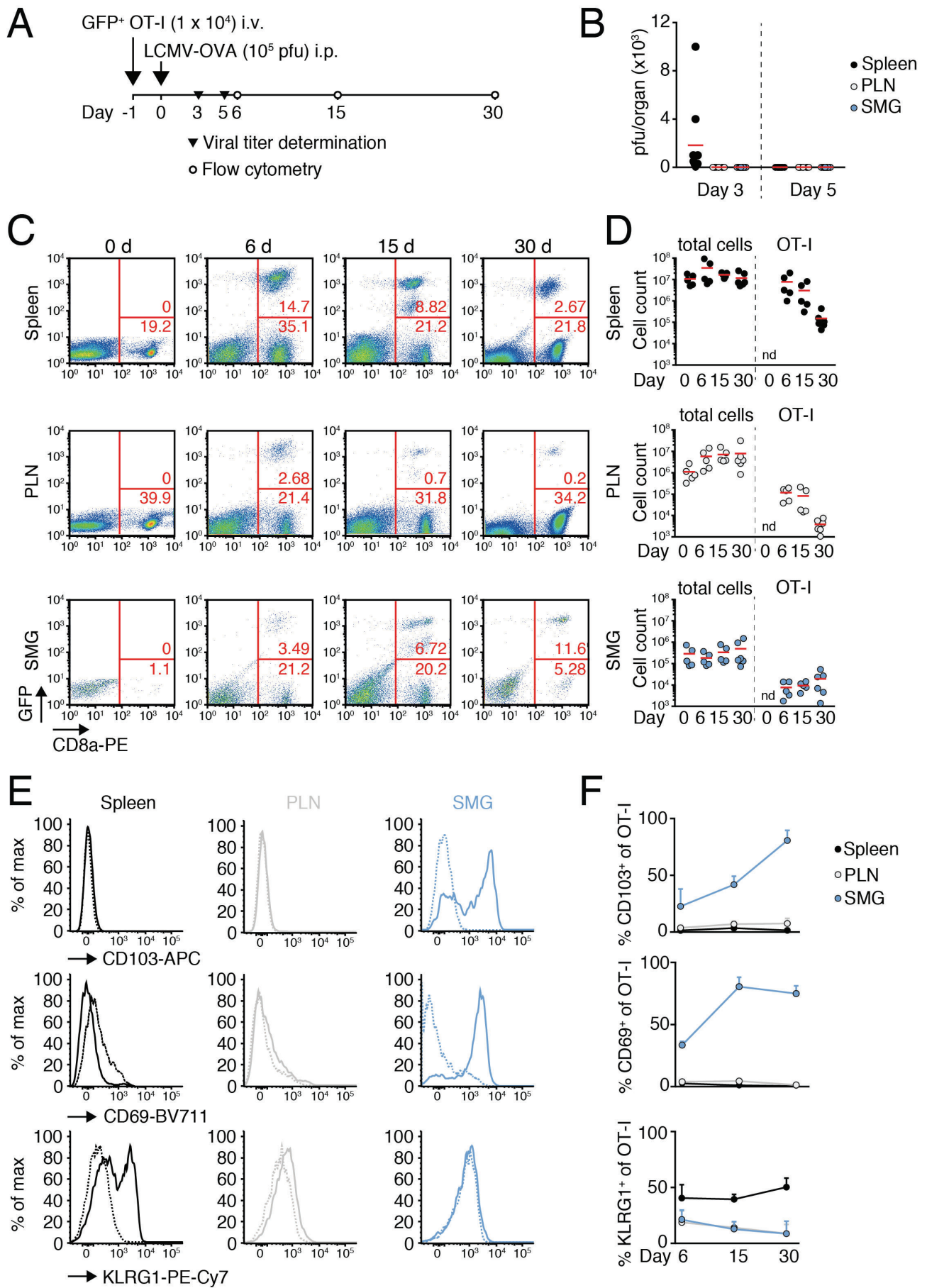
1343 **Movie S20. Time-lapse imaging of T_{RM} migration inside T_N cluster in presence of EDTA.** T_{RM} (green) show

1344 motility while traversing a cluster of T_N in presence of EDTA. Nuclei are labelled with Hoechst (blue). Major

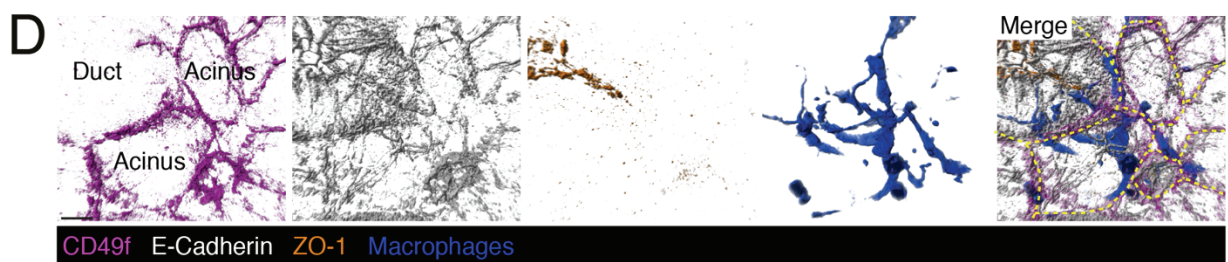
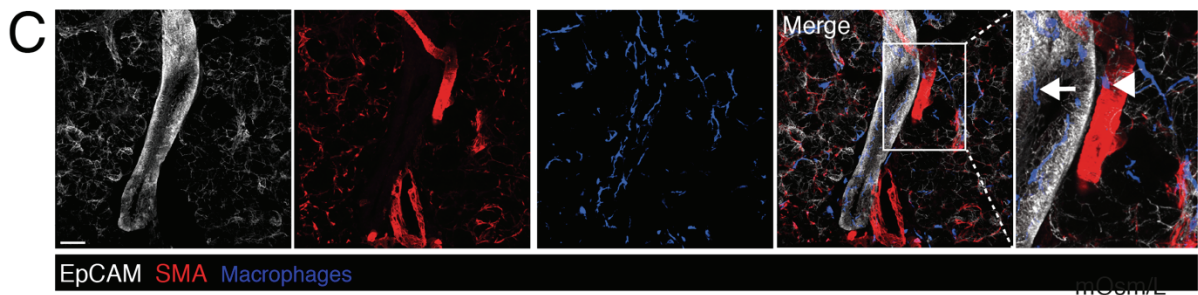
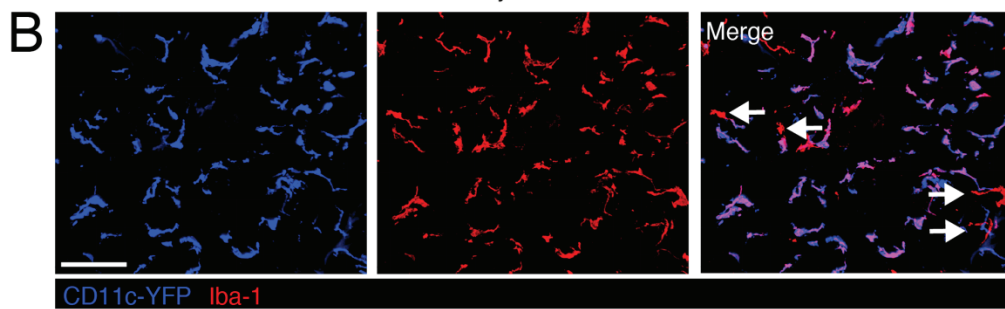
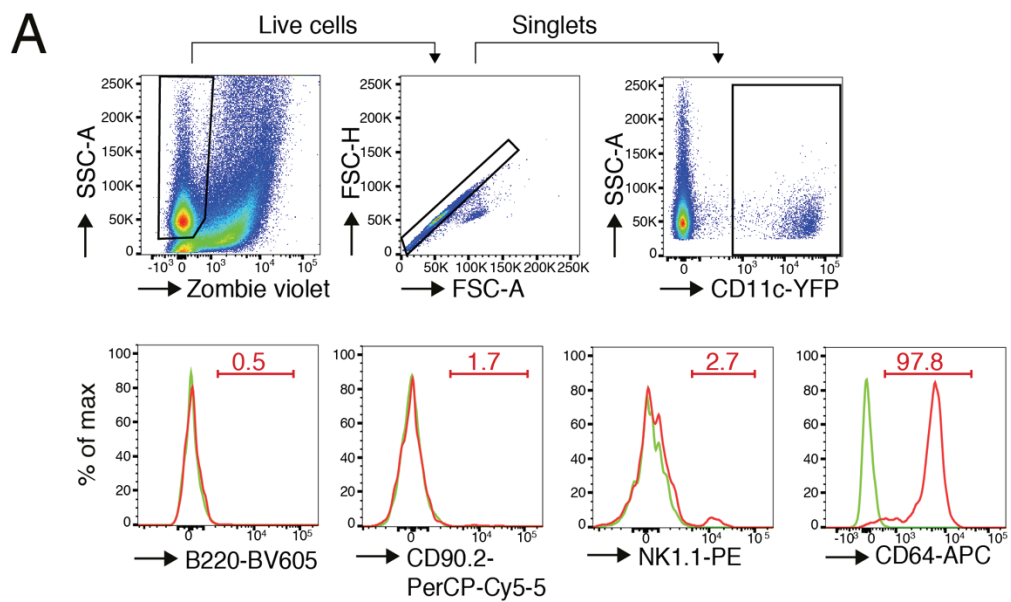
1345 ticks 5 μm . Time in min:s.

1346

1347 **Movie S21. Time-lapse imaging of T_{RM} migration along polystyrene beads in presence of EDTA. T_{RM} (green)**
1348 show motility while migrating in contact with polystyrene beads in presence of EDTA. Scale bar, 20 μm . Time
1349 in min:s.

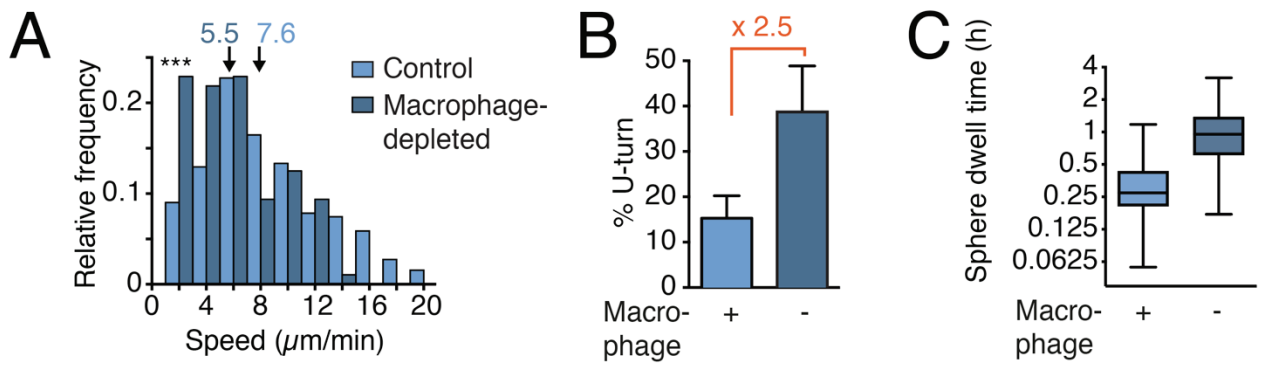


1350 Figure S1

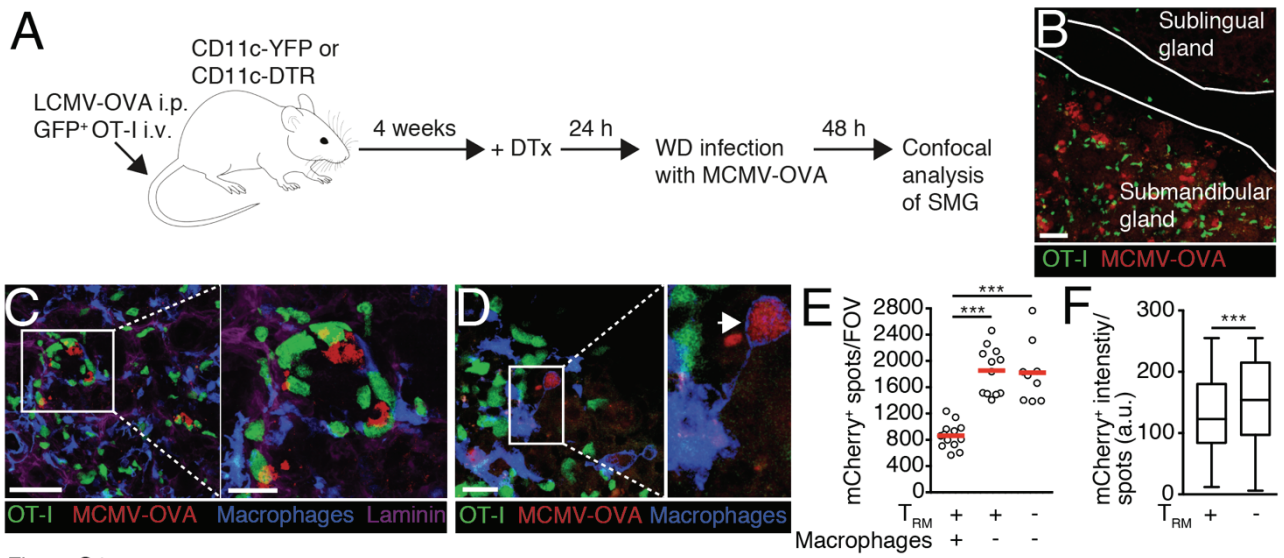


1351

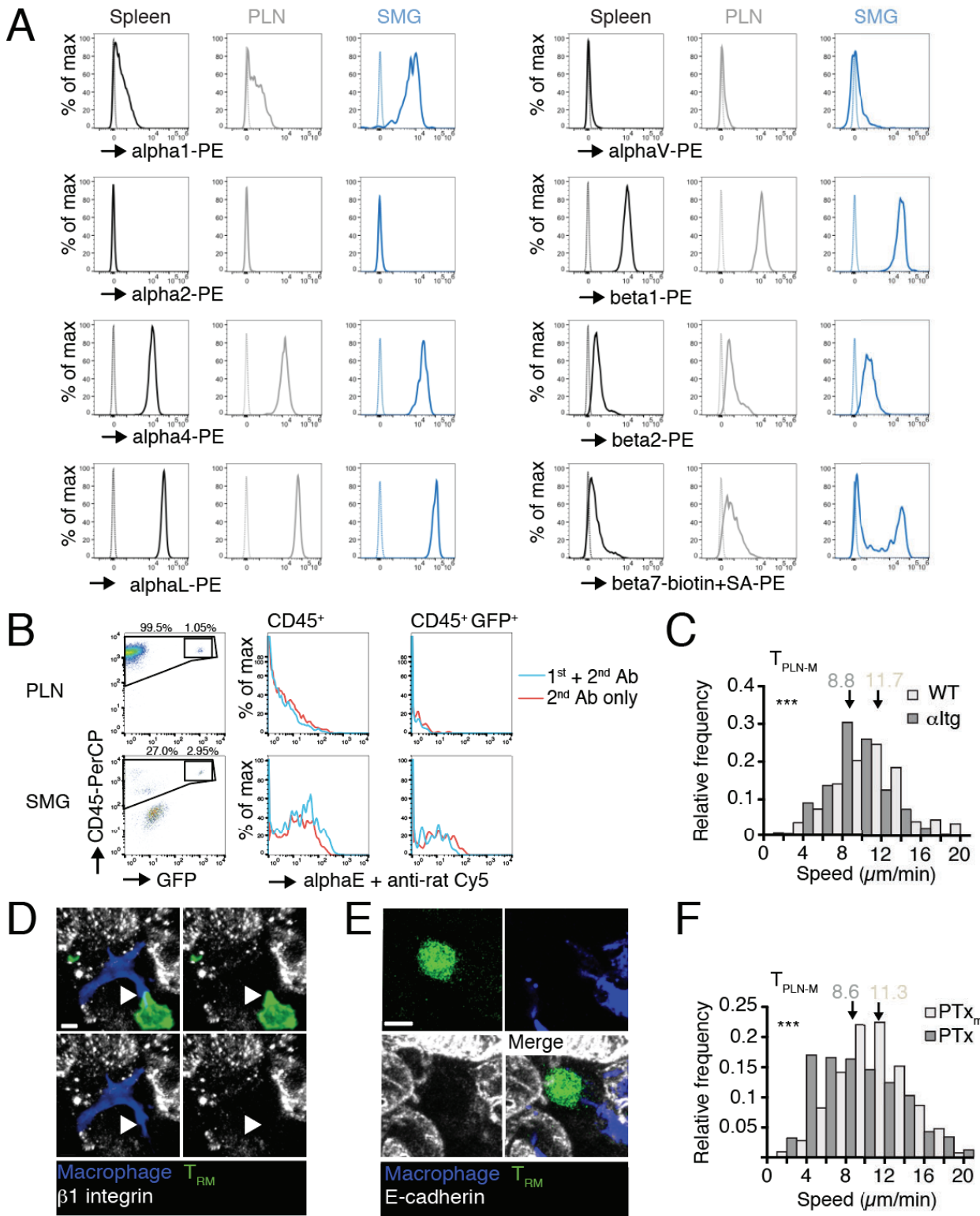
Figure S2



1352 Figure S3



1353 Figure S4



1354

Figure S5

1355